Metalorganic Chemical Vapor Deposition of α-Ga_2O_3 and α-$(Al_xGa_{1-x})_2O_3$ thin films on m-plane sapphire substrates

A F M Anhar Uddin Bhuiyan[1,a)], Zixuan Feng[1], Hsien-Lien Huang[2], Lingyu Meng[1], Jinwoo Hwang[2], and Hongping Zhao[1,2,b)]

[1]*Department of Electrical and Computer Engineering, The Ohio State University, Columbus, OH 43210, USA*

[2]*Department of Materials Science and Engineering, The Ohio State University, Columbus, OH 43210, USA*

[a)]Email: bhuiyan.13@osu.edu [b)]Corresponding author Email: zhao.2592@osu.edu

Abstract

Single α phase $(Al_xGa_{1-x})_2O_3$ thin films are grown on m-plane sapphire (α-Al_2O_3) substrates via metalorganic chemical vapor deposition (MOCVD). By systematically tuning the growth parameters including the precursor molar flow rates, chamber pressure and growth temperature, the epitaxial growth of high-quality phase pure α-$(Al_xGa_{1-x})_2O_3$ films ($0 \leq x \leq 1$) are demonstrated with smooth surface morphologies and alloy homogeneities by comprehensive material characterization. The asymmetrical reciprocal space mapping (RSM) reveals fully relaxed films for α-$(Al_xGa_{1-x})_2O_3$ films with $x \leq 0.5$. The coherent growth of α-$(Al_xGa_{1-x})_2O_3$/α-Al_2O_3 superlattice (SL) structures are demonstrated with abrupt interfaces and uniform Al distribution for higher Al composition at $x = 0.78$ in α-$(Al_xGa_{1-x})_2O_3$ layer. Influence of the growth parameters such as the growth temperature and chamber pressure on the phase stabilization and Al incorporation in the α-$(Al_xGa_{1-x})_2O_3$ films are investigated. While lower growth temperatures facilitate the phase stabilization of α-Ga_2O_3 thin films, lower chamber pressure leads to higher Al incorporation in α-$(Al_xGa_{1-x})_2O_3$ films. High resolution x-ray spectroscopy (XPS) was utilized for determining the Al compositions and bandgaps of α-$(Al_xGa_{1-x})_2O_3$. Furthermore, the evolution of the valance and conduction band offsets at α-Al_2O_3/α-$(Al_xGa_{1-x})_2O_3$ heterojunctions are evaluated with the variation of Al compositions which reveals the formation of type-I (straddling) band alignment between α-Al_2O_3 and α-$(Al_xGa_{1-x})_2O_3$.

Keywords: Ultra-wide bandgap, corundum α-$(Al_xGa_{1-x})_2O_3$ thin film, m-plane sapphire, metalorganic chemical vapor deposition (MOCVD)

I. Introduction

Gallium oxide (Ga_2O_3), having five different polymorphs (α, β, γ, δ and ε) [1] and an ultra-wide bandgap energy (~4.5-5.3 eV) [2, 3], is a transparent semiconducting material promising for high-power electronics due to its high predicted breakdown field strength (~8 MV/cm) [3]. Among different polymorphs, monoclinic β-phase Ga_2O_3 has attracted the most attention in recent years because of its availability of single crystal native substrates [4], controllable n-type doping [5-7] and possibility for bandgap engineering by alloying with Al_2O_3 [9-21]. The recent demonstrations of the epitaxial growth of high-quality phase pure β-$(Al_xGa_{1-x})_2O_3$ ($x \leq 0.52$) alloys on differently oriented β-Ga_2O_3 substrates [9-15] and high performance β-$(Al_xGa_{1-x})_2O_3$/β-Ga_2O_3 ($x \leq 0.26$) heterostructure based modulation doped field-effect transistors (MODFETs) [18-21] promise this material's potential in applications such as integrated power electronics and radio-frequency electronics. While the performance of $(Al_xGa_{1-x})_2O_3/Ga_2O_3$ heterostructure based MODFET devices largely depends on the Al incorporation in β-$(Al_xGa_{1-x})_2O_3$ layers, the high Al composition β-$(Al_xGa_{1-x})_2O_3$ alloys are not energetically favorable due to the structural phase transformation and domain rotation [10,22,23], which impedes the pathway to achieve larger bandgap energy with higher band offsets at $(Al_xGa_{1-x})_2O_3/Ga_2O_3$ interface [12,24].

Only recently, metastable rhombohedral corundum structured α-Ga_2O_3 (space group $R\bar{3}C$), with a large bandgap of 5.3 eV [2], has generated substantial interest in the scientific community. This is because α-Ga_2O_3 thin films can be epitaxially grown on inexpensive isostructural sapphire substrates [2, 25-36] and its electrical conductivity can be controlled [25, 28]. Moreover, α-Ga_2O_3 can be alloyed with other corundum oxides (Fe_2O_3, Cr_2O_3, V_2O_3), which provides opportunities

for the formation of quantum heterostructures. The bandgap engineering of α-Ga_2O_3 by alloying with α-Al_2O_3 and α-In_2O_3 over a large bandgap interval (3.7-9.2 eV) [38,39] also extends the electronic and optoelectronic applications into new regimes that are currently unachievable by monoclinic β-$(Al_xGa_{1-x})_2O_3$ alloys due to the limited Al incorporation. The demonstration of α-Ga_2O_3 based Schottky diodes and MESFET devices have also revealed this material's immense potential in high power electronics and deep ultraviolet optoelectronics [40].

Considering the enormous possibilities of α-Ga_2O_3 and its alloys in high-power and high frequency electronic applications, several studies have been conducted on the epitaxial growth of α-Ga_2O_3 and α-$(Al_xGa_{1-x})_2O_3$ alloys by different growth techniques including mist chemical vapor deposition [2,27,28,31,35,41,42], molecular beam epitaxy (MBE) [30,32,36,43] and halide vapor-phase epitaxy (HVPE) [29,33]. Previously, homoepitaxial growth of α-Al_2O_3 thin films was successfully demonstrated by MBE [44] and PLD [45] on atomically regulated sapphire substrates. As single crystal α-Ga_2O_3 native substrates are not available yet due to its metastability in the ambient atmosphere, the heteroepitaxial growth of α-Ga_2O_3 and α-$(Al_xGa_{1-x})_2O_3$ alloys are mostly investigated on inexpensive sapphire substrates which possesses the same corundum structure. Despite of having a large lattice mismatch between α-Ga_2O_3 and α-Al_2O_3 [~4.8% (a-axis) and ~3.54% (c-axes), respectively [28,29,31]], the controllable doping of α-Ga_2O_3 on c- and m- plane sapphire substrates have been reported by using mist-CVD growth technique [27,28,46]. Heteroepitaxial growth of α-Ga_2O_3 and α-$(Al_xGa_{1-x})_2O_3$ alloys on different crystal planes of sapphire substrates (c- [2,26,27,29,31,33,35,36,41,42], a- [36,43], m- [28,32,43] and r- [30,34,43]) have been investigated by different growth methods. MBE growth of Nd (neodymium) doped α-$(Al_xGa_{1-x})_2O_3$ alloys have been studied with different Al concentrations on differently oriented sapphire substrates (r-, a-, and m- planes) for laser application [43]. The growth of undoped α-

$(Al_xGa_{1-x})_2O_3$ thin films on c-plane sapphire substrates by mist-CVD growth method has been reported with Al compositions up to 81% [41]. The mist CVD growth of α-Ga_2O_3 thin films on c-plane sapphire substrates have been demonstrated with lower edge dislocation density by using α-$(Al_xGa_{1-x})_2O_3$ as a quasi-composition-graded buffer layer [47]. Band discontinuities at mist CVD grown α-Ga_2O_3/α-$(Al_xGa_{1-x})_2O_3$ heterointerfaces grown on c-plane sapphire substrates were also determined by x-ray photoemission spectroscopy [42].

While most of the growths of α-Ga_2O_3 thin films are investigated on c-plane sapphire substrates, recent studies on the growth of α-Ga_2O_3 films on c-plane sapphire substrates have revealed the formation of a few-monolayer thick (~3 nm) α-Ga_2O_3 interlayer at the substrates and epilayer interface, which subsequently transforms to β-phase as a form of rotational domain due to a large in-plane lattice mismatch between α-Ga_2O_3 and sapphire substrate [26,36]. These studies indicated that the growth of phase pure α-Ga_2O_3 alloys on c- sapphire substrates are limited by the film thicknesses. However, on a-plane sapphire substrates with a relatively smaller in-plane lattice mismatch, the isomorphic phase stabilization of α-Ga_2O_3 up to a film thickness of 14.3 nm has been reported [36]. On the other hand, relatively thicker isomorphic α-Ga_2O_3 layers were grown on r- plane sapphire substrates with a thickness of 217 nm [30]. However, further increase of the film thicknesses leads to the nucleation of β-Ga_2O_3 with the epitaxial relationship of ($\bar{2}$01) β-Ga_2O_3 || (0001) α-Ga_2O_3 on c-plane facets that are exposed during the growth of α-Ga_2O_3 [30]. These studies imply that the growth of phase pure α-Ga_2O_3 and α-$(Al_xGa_{1-x})_2O_3$ alloys are highly dependent on the crystal orientations of sapphire substrates.

While achievable film thicknesses of phase pure α-Ga_2O_3 is limited due to the phase transition that occurs by the formation of c-plane facets on α-Ga_2O_3 surface during the growth on c- and r-plane sapphire, a crystal plane that is perpendicular to the c-plane such as a- or m-planes can

potentially promote the growth of phase pure α-Ga_2O_3 and α-$(Al_xGa_{1-x})_2O_3$ alloys by avoiding the formation of c-plane facets. Based on this principle, by using m-plane sapphire substrate, a recent MBE growth study have revealed a pathway to achieve phase pure (56-84.3 nm thick) α-$(Al_xGa_{1-x})_2O_3$ alloys for the entire Al composition range with bandgap energies of 5.4-8.6 eV [32]. Although controllable conductivity was not achieved by this MBE growth study, another work on the mist CVD growth of Sn doped α-Ga_2O_3 thin film grown on m-plane sapphire substrates was demonstrated with promising transport properties such as a room temperature mobility of 65 $cm^2/V.s$ at a high doping concentration of 1.2 x 10^{18} cm^{-3} [28]. Previously, the growth of phase pure α-$(Al_xGa_{1-x})_2O_3$ alloys and α-Ga_2O_3 films were also investigated on a-plane sapphire substrates by using MBE growth technique [36,43]. Although quite a few studies have been conducted on the epitaxial growth of α-Ga_2O_3 films and its alloy on differently oriented sapphire substrates by different growth techniques, MOCVD growths of α-Ga_2O_3 and α-$(Al_xGa_{1-x})_2O_3$ alloys are not reported yet.

In this study, for the first time, we investigated the MOCVD growth of α-Ga_2O_3 and α-$(Al_xGa_{1-x})_2O_3$ alloys on m-plane sapphire substrates for the entire Al composition range. The MOCVD grown α-Ga_2O_3/α-$(Al_xGa_{1-x})_2O_3$ superlattice structures with different Al compositions have also been studied. Moreover, the evolution of the band offsets at α-Al_2O_3/α-$(Al_xGa_{1-x})_2O_3$ heterointerfaces with the variation of Al compositions from 0% to 78% are also investigated by XPS measurement. The crystalline structure and quality of the epi-films, strain characteristics, compositional homogeneity, surface morphology and the band gaps of α-$(Al_xGa_{1-x})_2O_3$ are evaluated by comprehensive characterization via x-ray diffraction (XRD), high resolution scanning transmission electron microscopy (HR STEM), energy dispersive x-ray spectroscopy (EDX), x-ray photoelectron spectroscopy (XPS), atomic force microscopy (AFM), field emission

scanning electron microscopy and Raman spectroscopy, which reveal the high quality epitaxial growth of α-Ga_2O_3 and α-$(Al_xGa_{1-x})_2O_3$ alloys on m-plane sapphire substrates via MOCVD.

II. Experimental Section

II.A. MOCVD growth

α-Ga_2O_3 and α-$(Al_xGa_{1-x})_2O_3$ thin films were grown on m-plane sapphire substrates by using Agnitron Agilis MOCVD reactor. Trimethylaluminum (TMAl) and Triethylgallium (TEGa) were used as Al and Ga precursors, respectively. Pure O_2 gas was used as O-precursor and Argon (Ar) was used as the carrier gas. The growth temperature was varied from 650 °C to 880 °C. The reactor pressure was tuned between 20 torr and 80 torr. TEGa molar flow rate was varied from 0 (for Al_2O_3 growth) to 19.12 μmol min^{-1}, while the TMAl molar flow rate was adjusted from 0 (for Ga_2O_3 growth) to 11.59 μmol min^{-1}. The O_2 molar flow rate was kept constant at 500 sccm. The growth rate was varied from 0.27-1.33 μm/hr for α-$(Al_xGa_{1-x})_2O_3$ thin films with various Al composition. Prior loading the substrates into the growth chamber, the substrates were ex-situ cleaned by using solvents. High temperature in-situ cleaning under O_2 atmosphere for 5 mins at 920 °C was performed prior to the initiation of the epitaxial growth.

II.B. Materials characterization

The Al compositions, crystalline structure and quality of the films were evaluated by XRD measurements using a Bruker D8 Discover with Cu Kα radiation x-ray source (λ =1.5418 Å). The strain characteristics of the films were investigated by XRD asymmetrical reciprocal space mapping for different Al compositions. Field emission scanning electron microscopy (FESEM, FEI Helios 600) and atomic force microscopy (AFM, Bruker AXS Dimension Icon) were used to characterize the surface morphology and the surface roughness, respectively. Room temperature

Raman spectroscopy was performed by using a laser beam of 514 nm (Renishaw−Smiths Detection Combined Raman-IR Microprobe). To confirm the Al compositions and to estimate the bandgap energies, XPS measurements were performed by using Kratos Axis Ultra X-ray photoelectron spectrometer with a monochromatized Al Kα x-ray source (E_{photon} = 1486.6 eV). The band offsets at α-Al_2O_3/α-$(Al_xGa_{1-x})_2O_3$ heterointerfaces for different Al compositions were also determined by utilizing XPS with an energy resolution of 0.1 eV. The electron pass energy was set at 20 eV for high resolution scans and 80 eV for the survey scans. C 1s core level at 284.8 eV was used to calibrate the binding energy. A Thermo Fisher Scientific Titan scanning transmission electron microscopy, operated at 300 kV, was used to obtain high angle annular dark field (HAADF) STEM images and EDS spectral mapping. Film thicknesses were obtained from the cross-sectional FESEM and STEM HAADF images as well as from STEM-EDS elemental mapping profile of α-$(Al_xGa_{1-x})_2O_3$ thin films.

III. Results and Discussions

In order to evaluate the crystalline structure, quality and the strain state of the α-$(Al_xGa_{1-x})_2O_3$ thin films, high resolution XRD was performed for different Al compositions. Figure 1(a) shows the XRD ω-2θ scans of the α-$(Al_xGa_{1-x})_2O_3$ thin films grown on m-plane sapphire substrate. The films were grown by systematically tuning the [TMAl]/[TEGa+TMAl] molar flow rate ratios from 0% to 100%. The optimized growth conditions such as the TEGa and TMAl molar flow rates, growth temperature and chamber pressure for the growth of α-Ga_2O_3 and α-$(Al_xGa_{1-x})_2O_3$ films with different Al compositions are listed in Table 1. High intensity prominent diffraction peaks from $(30\bar{3}0)$ reflection of α-$(Al_xGa_{1-x})_2O_3$ are observed with the same crystal orientation as the substrate, as shown in the XRD spectra in Figure 1(a). The Al compositions of α-$(Al_xGa_{1-x})_2O_3$ films, ranging from 0% to 100%, are determined by calculating the interplanar distance between α-Al_2O_3

substrate and α-Ga_2O_3 epi-film from the XRD peak positions of α-Al_2O_3 and α-Ga_2O_3. As the Al molar flow rate increases, the peak corresponding to $(30\bar{3}0)$ reflection of α-$(Al_xGa_{1-x})_2O_3$ shifts toward the α-Al_2O_3 substrate peak, indicating the reduction of the lattice mismatch between the substrate and the epi-film. No other peaks are observed from the ω-2θ scan in a wide 2θ range. The single crystallinity of the films is also confirmed by the XRD φ-scan of the off-axis $(22\bar{4}0)$ diffractions from α-$(Al_xGa_{1-x})_2O_3$. Only twofold rotational symmetry was observed from the $(22\bar{4}0)$ φ-scans for both 78% and 0% Al composition samples as shown in Figure 2(b), implying the absence of any rotational domains. Figure 1(c) shows the full width at half maximum (FWHM) omega rocking curve (RC) for $(30\bar{3}0)$ α-$(Al_xGa_{1-x})_2O_3$ reflections for different Al compositions. RC FWHM values decrease with the increase of Al compositions, indicating better crystalline quality of the films for higher Al composition samples, which can be attributed to the reduced lattice mismatch between substrate and epilayers due to higher Al incorporation.

Unlike the mist-CVD growth of α-Ga_2O_3 on c-plane sapphire substrates where the growth of high-quality single crystalline α-Ga_2O_3 thin films was found to be difficult due to the appearance of the c-plane facets on Ga_2O_3 surface [26, 36], the phase control of α-Ga_2O_3 and $(Al_xGa_{1-x})_2O_3$ has been successfully attained by MOCVD on m-plane sapphire substrates. The c-plane facets formed on the growth surface lead to the phase transformation. Previous efforts on the growth of α-Ga_2O_3 films on c-plane sapphire substrates showed the transition from α- to β-phase with an epitaxial relationship of $(\bar{2}01)$ β-Ga_2O_3 || (0001) sapphire as the film exceeds a few nanometers of thickness [26, 36]. In case of the growth on r-plane, relatively thicker α-Ga_2O_3 films were found to be stabilized as c-plane remains at an angle with the growth plane [30]. That study demonstrated that the phase stability can be maintained until the c plane facets are formed on the growth surface. On the other hand, m-plane of the sapphire substrates is perpendicular to the c-plane, and thus

prevents the possibility of the c-plane facet formations during the growth, allowing phase pure α-Ga_2O_3 epitaxy on m-plane sapphire substrates [32]. While the use of m-plane sapphire substrates primarily promotes the growth of phase pure α-Ga_2O_3 and $(Al_xGa_{1-x})_2O_3$, the MOCVD growth conditions such as the growth temperature, [TMAl]/[TMAl+TEGa] molar flow ratio and chamber pressure also influence the phase stability of α-Ga_2O_3 and α-$(Al_xGa_{1-x})_2O_3$, as discussed in later sections.

To investigate the strain state of the epitaxial films, asymmetrical reciprocal space mapping (RSM) was performed on α-$(Al_xGa_{1-x})_2O_3$ films for different Al compositions. Figures 2 (a)-(d) show the asymmetrical RSMs for $(22\bar{4}0)$ reflections of α-$(Al_xGa_{1-x})_2O_3$ films with 0%, 15%, 50% and 78% Al compositions. The fully relaxed and strained positions are shown by the tilted and vertical black dashed lines, respectively. The maximum reflection intensity of $(22\bar{4}0)$ α-$(Al_xGa_{1-x})_2O_3$ reciprocal lattice point (the out-of-plane reciprocal space lattice constant, Q_z) moves closer to α-Al_2O_3 substrate peak as the Al composition increases. Fully relaxed α-$(Al_xGa_{1-x})_2O_3$ films are observed for the Al compositions of 0%, 15% and 50% [Figures 1 (a)-(c)], as indicated by the alignment of the $(22\bar{4}0)$ α-$(Al_xGa_{1-x})_2O_3$ peak positions on the fully relaxed line (tilted dashed lines). However, for the sample with Al composition of 78% as shown in Figure 2 (d), the $(22\bar{4}0)$ peak position of α-$(Al_xGa_{1-x})_2O_3$ shifts toward the fully strained line, indicating the existence of compressive strain in α-$(Al_xGa_{1-x})_2O_3$ films for higher Al compositions (partial relaxation).

The surface morphology and roughness of α-$(Al_xGa_{1-x})_2O_3$ films for the Al compositions spanning between 0% and 100% were evaluated by FESEM [Figures S1(a)-(j) in Supplementary material] and AFM imaging with a scan area of 5μm by 5μm as shown in Figures 3(a)-(j). All the

films with different Al compositions show smooth and uniform surface morphologies as observed from the FESEM images in Supplementary material. The surface RMS roughness of α-$(Al_xGa_{1-x})_2O_3$ films for different Al compositions range between 0.79 nm and 3.12 nm. The general trend shows that the surface roughness decreases with the increase of the Al compositions. As the Al composition increases from 0% to 58%, the RMS roughness decreases from 3.12 nm to 1.33 nm as shown in Figures 3(a)-(g). However, relatively thicker α-$(Al_xGa_{1-x})_2O_3$ films with 68% and 78% Al compositions show slightly higher RMS values as shown in Figures 3(h) and (i), which can be related to the growth conditions such as the precursor molar flow rates and relatively higher thicknesses of the films as listed in Table 1. Nevertheless, the homoepitaxial α-Al_2O_3 film exhibits very smooth surface morphology with RMS roughness of 0.79 nm as shown in Figure 3(j).

Room temperature Raman spectra of the α-$(Al_xGa_{1-x})_2O_3$ films grown on m-plane sapphire substrates with different Al compositions ranging between 0% and 100% are shown in Figure 4. Raman spectrum of a single crystal m-plane sapphire substrate are also included in the figure. A single crystal sapphire with the a- and m-axes perpendicular to the c-axis possesses trigonal symmetry. Among all the vibrational modes (Raman active, infrared active or acoustic) of the sapphire corundum crystal, only two A_{1g} modes and five E_g modes are Raman active [48,49]. We could resolve six different Raman bands (two A_{1g} and four E_g) from the α-$(Al_xGa_{1-x})_2O_3$ films for different Al compositions, which agree well with the Raman modes of the m-plane sapphire crystal [48,49]. In the recorded Raman spectra as shown in Figure 4, the bands at around 417 and 645 cm^{-1} belong to the A_{1g} vibrational mode and the peaks at around 378, 430, 578, and 750 cm^{-1} can be assigned to the E_g mode. The Raman spectra of the α-$(Al_xGa_{1-x})_2O_3$ for all investigated Al compositions show very similar features as compared to the spectrum of the sapphire substrates without any obvious Raman shifts, suggesting that the symmetry of the α-$(Al_xGa_{1-x})_2O_3$ crystal

structures are well maintained. While very low intensity E_g mode located at 750 cm^{-1} are observed for all the Al compositions investigated, the E_g mode at 578 cm^{-1} cannot be identified for lower Al composition samples (0%-36%), which can be attributed to the higher strain relaxation of the epi-films due to the increase in the lattice mismatches.

To investigate the influence of the growth temperature and chamber pressure on the epitaxial growth, two α-Ga_2O_3 films grown at growth temperatures of 650°C and 880°C (at 20 torr chamber pressure) and two α-$(Al_xGa_{1-x})_2O_3$ films grown with the same [TMAl]/[TMAl+TEGa] molar flow ratio (49.24%) at different chamber pressures of 20 and 80 torr (880°C) were compared by XRD ω-2θ scan profiles as shown in Figures 5(a) and (b). The growth of phase pure α-Ga_2O_3 on m-plane sapphire substrates was observed at growth temperature of 650°C [Figure 5(a)(ii)]. However, at relatively higher growth temperature (880°C), the film exhibits the co-existence of both α and β phases, as indicated by XRD diffraction peaks from $(30\bar{3}0)$ α-Ga_2O_3 and (020) β-Ga_2O_3 [Figure 5(a)(i)], suggesting that the phase pure α-Ga_2O_3 can be stabilized at lower temperature. Previous study on mist-CVD growth of α-Ga_2O_3 films on c-plane sapphire substrates reported that the α-Ga_2O_3 films remain stable up to 660°C and the phase stability of α-Ga_2O_3 can be extended up to 1100°C by alloying with Al [50]. In our study, although α-Ga_2O_3 films grown at higher temperature exhibited phase transformation, α-$(Al_xGa_{1-x})_2O_3$ films are found to remain stable up to 880°C for all the Al compositions investigated. While the growth temperature showed strong influence on the phase stability of α-Ga_2O_3, the Al incorporation in α-$(Al_xGa_{1-x})_2O_3$ films are found to have strong dependence on the growth chamber pressure. With the same [TMAl]/[TMAl+TEGa] malar flow ratio of 49.24%, the Al composition decreased from 78% to 60% as the chamber pressure increased from 20 to 80 torr [Figure 5(b)], indicating that the higher

chamber pressure led to the lower Al incorporation in α-$(Al_xGa_{1-x})_2O_3$ films. This can be ascribed to the increase of the gas phase reaction of precursors due to the increase of chamber pressure [5].

In order to investigate the impact of the film thicknesses on the strain state and the surface morphologies, four α-$(Al_xGa_{1-x})_2O_3$ films (x = 50%) with targeted thickness of 75 nm, 30 nm, 15 nm and 7.5 nm were grown. The strain state of the epitaxial films was characterized by asymmetrical reciprocal space mapping (RSM) as shown in Figure 6. The 75 nm thick α-$(Al_{0.50}Ga_{0.50})_2O_3$ film is found to be fully relaxed as evidenced by the alignment of the epi-film peak on fully relaxed (tilted) line [Figure 6(a)]. As the film thickness reduces from 75 nm to 15 nm, the α-$(Al_{0.50}Ga_{0.50})_2O_3$ layer peak starts to shift toward the fully stained (vertical) line, indicating the epi-films are partially relaxed [Figure 6(b) and (c)]. Meanwhile, the peak from the 7.5 nm thick α-$(Al_{0.50}Ga_{0.50})_2O_3$ film is found to be aligned vertically to the substrate peak indicating the same Q_x value as shown in Figure 6(d), which confirms that the 7.5 nm thick α-$(Al_{0.50}Ga_{0.50})_2O_3$ layer has the same in-plane lattice constant as the sapphire substrate, indicating a fully coherent growth of α-$(Al_{0.50}Ga_{0.50})_2O_3$ up to a thickness of 7.5 nm. The surface roughnesses of α-$(Al_{0.50}Ga_{0.50})_2O_3$ films are also investigated by AFM imaging as a function of film thicknesses as shown in Figure S2 of the supplementary material. The surface roughness monotonically reduces from 1.72 nm to 0.39 nm, as the film thicknesses decreases from 75 nm to 7.5nm, indicating the film thicknesses have a strong influence on the surface morphology.

The crystalline structure of α-Ga_2O_3 and α-$(Al_xGa_{1-x})_2O_3$ films with different Al compositions were investigated using high-resolution STEM imaging. Figures 7 (a)-(f) show the atomic resolution HAADF-STEM images for α-$(Al_xGa_{1-x})_2O_3$ films with 0% [Figures 7 (a)-(b)], 50% [Figures 7 (c)-(d)] and 78% [Figures 7 (e)-(f)] Al compositions. Zero percent Al composition sample (α-Ga_2O_3) was imaged from <0001> zone axis and α-$(Al_xGa_{1-x})_2O_3$ films with 50% and

78% Al compositions were imaged from <$12\bar{3}\bar{1}$> zone axis. Undisturbed α-phase structures without noticeable compositional segregation or phase transformation were observed from the STEM images from all Al compositions. The sharp contrasts between the α-Al_2O_3 substrates (dark) and α-$(Al_xGa_{1-x})_2O_3$ epi-films (bright) indicate high quality α-Al_2O_3/α-$(Al_xGa_{1-x})_2O_3$ interfaces. However, at higher magnification, α-Ga_2O_3 films exhibit less abrupt interface due to the large lattice mismatch between the substrate and the epi-layer [Figures 7(b)] as compared to the 50% and 78% Al composition samples [Figures 7(d) and (f)]. For all three samples, the epilayers show slight contrast variations, especially near the interface, which can be related to the strain relaxation of the films. Dislocations, such as threading dislocations, can be seen as dark and vertical lines stemming from the interface toward the top of the film as shown in the HAADF STEM image in Figure 7(a), where there exists high level of strain between α-Ga_2O_3 and α-Al_2O_3. We see less dislocations in other samples (x=50 and 78%), which is expected since there exists less strain in those samples. The evidence of strain at the interface and its relaxation can also be found in the HAADF STEM image in Figure 7(a). The interface region (near the dashed line) has darker contrast, which should be the result of de-channeling of the incoming electrons due to the strain near the interface. The darker region vertically extends by about a few nanometers, which suggests that the lattice relaxes within a few nanometers of the film. The x = 50% or x = 78% samples, on the other hand, do not show such strain (i.e. dark contrast at the interface) or its relaxation at or near the interface.

Additionally, energy dispersive x-ray spectroscopy (STEM-EDS) was performed to estimate the Al compositions and evaluate the chemical homogeneity throughout the entirety of the α-Ga_2O_3 and α-$(Al_xGa_{1-x})_2O_3$ films with different Al compositions (Figures 8). Figures 8 (a)(e)(i) show the cross sectional HAADF STEM images taken for 0%, 50% and 78% Al samples.

The film thicknesses estimated from the cross-sectional STEM images are found to be 85 nm, 150 nm and 200 nm for Al composition of 0%, 50% and 78%, respectively, which show a good agreement with those extracted from the SEM cross-sectional images. The EDS color maps of Ga (blue) and Al (green) elements in Figures 8(b)-(c) [0% Al], 8(f)-(g) [50% Al] and 8(j)-(k) [78% Al] reveal the abrupt interfaces with chemical homogeneity of the films for different Al compositions. The line scan along the film thickness direction [orange lines in Figures 8(a), (e), and (f)] provides the concentration of each element, as shown in Figures 8(d), (h), and (l), respectively. All the samples show uniform and homogeneous distribution of Al and Ga throughout the films. The average Al compositions estimated from the STEM-EDS elemental maps show a good agreement with those extracted from the XRD measurements.

In addition to the growth of α-$(Al_xGa_{1-x})_2O_3$ thin films, we also investigated the growth of α-Al_2O_3/α-$(Al_xGa_{1-x})_2O_3$ superlattice (SL) structures by varying the Al compositions. Figure 9(a) shows the schematic of 8 periods α-Al_2O_3/α-$(Al_xGa_{1-x})_2O_3$ SL structure grown with 78% Al composition. The targeted thickness of each period was 25 nm consisting of a 15 nm thick α-Al_2O_3 barrier and a 10 nm thick α-$(Al_xGa_{1-x})_2O_3$ well layers. The structural quality, strain and the interfacial abruptness were evaluated by XRD ω-2θ and RSM scans as shown in Figures 9(b) and (c), respectively. High intensity, sharp and distinguishable high order satellite peaks (up to 5^{th} order) were observed from the ω-2θ scans, indicating the growth of high-quality SL structures with abrupt interfaces with 78% Al compositions. The asymmetrical RSM map of $(22\bar{4}0)$ reflections from α-Al_2O_3/α-$(Al_xGa_{1-x})_2O_3$ SL structures are shown in Figure 9(c). All the peaks originated from the SL satellites are found to align vertically with the α-Al_2O_3 substrate peak, suggesting the same Q_x value which confirm the coherent growth of fully strained α-$(Al_xGa_{1-x})_2O_3$ SL structure grown on m-plane sapphire substrate.

The structural and interfacial quality of the α-$(Al_xGa_{1-x})_2O_3$/α-Al_2O_3 and α-$(Al_xGa_{1-x})_2O_3$/α-Ga_2O_3 SL structures grown with different Al compositions were also evaluated by atomic resolution STEM imaging. Figures 10 (a,e) and (b,f) show the HAADF-STEM images taken for α-$(Al_xGa_{1-x})_2O_3$/α-Al_2O_3 SL structures grown with 78% and 50% Al compositions in α-$(Al_xGa_{1-x})_2O_3$ layers, respectively. Similarly, α-$(Al_xGa_{1-x})_2O_3$/α-Ga_2O_3 SL structures grown with 50% and 17% Al compositions are shown in Figures 10 (c,g) and (d,h), respectively. The STEM images confirm the growth of 8 periods alternating SLs, maintaining the α-phase throughout the entire structures. The SL structure grown with 78% Al composition as shown in Figures 10 (a,e) exhibits relatively sharp interfaces between α-$(Al_xGa_{1-x})_2O_3$ and α-Al_2O_3 layers with a decent structural homogeneity. The SLs grown with 50% Al compositions as shown in Figures 10 (b,f) and (c,g) also maintain fair quality at the interface, although less sharp than the 78% SLs. The α-$(Al_xGa_{1-x})_2O_3$/α-Ga_2O_3 SL with 17% Al compositions in α-$(Al_xGa_{1-x})_2O_3$ layer show more inhomogeneous interface [Figures 10 (d,h)].

The STEM-EDS maps of the corresponding SL structures are shown in Figures 11 (a-p). The cross sectional HAADF STEM images for α-$(Al_xGa_{1-x})_2O_3$/α-Al_2O_3 SLs with 78% and 50% Al compositions and α-$(Al_xGa_{1-x})_2O_3$/α-Ga_2O_3 SLs with 50% and 17% Al compositions are shown in Figures 11 (a), (e), (i) and (m), respectively. The EDS color maps of Ga (blue) and Al (green) components in Figures 11 (b,c), (f,g), (j,k) and (n,o) correspond to the Ga and Al concentrations of Figures 11(d), (h), (l) and (p) for different SLs with different Al compositions. The elemental plots in Figures 11(d), (h), (l) and (p) show the alternating compositional profiles of the periodic structures. Although the periodicities of the SL structures are found to be maintained for all the SLs, the alloy homogeneity and the interface abruptness reduces as the Al compositions in the α-$(Al_xGa_{1-x})_2O_3$ layers decrease. The average Al composition estimated from the STEM-EDS

elemental maps for different SL structures closely match with the targeted Al compositions in α-$(Al_xGa_{1-x})_2O_3$ layers.

The elemental compositions and the band gaps of α-$(Al_xGa_{1-x})_2O_3$ thin films and the band offsets at α-Al_2O_3/α-$(Al_xGa_{1-x})_2O_3$ heterojunctions are estimated by using high resolution XPS. The XPS survey spectra as shown in Figure S3 of the supplementary materials for α-$(Al_xGa_{1-x})_2O_3$ films with different Al compositions exhibit no metallic contaminants in the films, indicating the growth of highly pure α-$(Al_xGa_{1-x})_2O_3$ films on m-plane sapphire for the whole Al composition range. The Al compositions in the films were estimated by using the areas of Ga 3s, Al 2s and Al 2p core level spectra by using their corresponding sensitivity factors of $S_{Ga\ 3s} = 1.13$, $S_{Al\ 2s} = 0.753$, $S_{Al\ 2p} = 0.5371$ after applying the Shirley background subtraction. The detail calculations of Al compositions in α-$(Al_xGa_{1-x})_2O_3$ films using XPS measurements are listed in Table S1 of the supplementary materials. The Al compositions determined by XPS measurements correlate well with those estimated from XRD and STEM-EDS mapping.

By utilizing XPS, the bandgap energies of the α-$(Al_xGa_{1-x})_2O_3$ thin films were also determined for different Al compositions. The bandgap energies of wide bandgap semiconductor materials can be extracted by analyzing the onset of inelastic spectrum at the higher binding energy side of a strong intensity core level peak [42,51,52]. As the energetically lowest inelastic scattering that an electron experiences on its way to the surface is its excitation from the valance band to the conduction band, the fundamental lower limit of the inelastic scattering corresponds to the bandgap of the material [51]. In this study, for the bandgap determination, Ga $2p_{3/2}$ core levels were used for α-$(Al_xGa_{1-x})_2O_3$ thin films (x = 0% - 78%) and O 1s core level was used for α-Al_2O_3 film (x = 100%), as exemplarily shown in Figures 12 (a)-(c) for α-$(Al_xGa_{1-x})_2O_3$ films with 0% and 50% and α-Al_2O_3 film, respectively. The inset of each figure represents the zoomed view of the

background region of the core levels. The onset of inelastic loss spectra was determined from the intersection of the linear extrapolation of the loss spectra curve to the constant background. By measuring the onset of inelastic background relative to the Ga $2p_{3/2}$ [Figures 12(a) and (b)] and O 1s core [Figure 12(c)] level peaks, the bandgap energies of α-Ga_2O_3, α-$(Al_{0.50}Ga_{0.50})_2O_3$ and α-Al_2O_3 thin films were calculated as 5.41 ± 0.15 eV, 6.45 ± 0.15 eV, and 8.81 ± 0.15 eV, respectively. The bandgaps of other Al composition samples were also determined by similar approach, as listed in Table 2. The error bars correspond to the standard deviation of the estimated onset of inelastic losses. Figure 12 (d) shows the bandgaps of α-$(Al_xGa_{1-x})_2O_3$ films as a function of Al composition. With the increase of the Al compositions, the bandgaps of α-$(Al_xGa_{1-x})_2O_3$ were found to increase monotonically from 5.41 eV (α-Ga_2O_3) to 8.81 eV (α-Al_2O_3). The experimental bandgap energies extracted in this study by using XPS are in a close agreement with the theoretically predicted bandgap values based on first-principles hybrid density functional theory (DFT) [8]. The bowing parameter (b) extracted from the quadratic fitting of the bandgap values was found to be 2.16 eV, which matches well with the theoretically calculated value [1.78 eV (indirect) and 1.87 eV (direct) [53]].

The band offsets are considered as critical material properties for semiconductor heterostructure device design. In this study by utilizing XPS, we have also measured the band offsets at α-$(Al_xGa_{1-x})_2O_3$/α-Al_2O_3 heterojunctions for the entire Al composition range. Three types of samples were prepared for the band offset measurement as shown in the schematics of Figure S4 in supplementary materials: 50 nm thick (a) α-Al_2O_3 and (b) α-$(Al_xGa_{1-x})_2O_3$ layers with 0%, 50% and 78% Al compositions directly grown on m-plane sapphire substrate, and (c) thin (2 nm) layer of α-$(Al_xGa_{1-x})_2O_3$ [x = 0%, 50% and 78%] grown on 50 nm thick α-Al_2O_3 layer on top of sapphire substrate for capturing all the electronic states from the α-$(Al_xGa_{1-x})_2O_3$/α-Al_2O_3

interfaces. The Kraut's method was employed for the determination of the valance (ΔE_v) and conduction (ΔE_c) band offsets as follows [54].

$$\Delta E_v = (E^{AlGaO}_{Ga\ 3s} - E^{AlGaO}_{VBM}) - (E^{AlO}_{Al\ 2p} - E^{AlO}_{VBM}) - (E^{AlGaO/AlO}_{Ga\ 3s} - E^{AlGaO/AlO}_{Al\ 2p}) \quad (1)$$

$$\Delta E_c = E^{AlO}_g - E^{AlGaO}_g - \Delta E_v \quad (2)$$

Here, the energies of the valance band minimum and Ga 3s core levels for α-$(Al_xGa_{1-x})_2O_3$ are defined as E^{AlGaO}_{VBM} and $E^{AlGaO}_{Ga\ 3s}$, respectively. Similarly, E^{AlO}_{VBM} and $E^{AlO}_{Al\ 2p}$ represent the valance band minimum and the Al 2p core levels for α-Al_2O_3. The Ga 3s and Al 2p core levels from the α-$(Al_xGa_{1-x})_2O_3$/α-Al_2O_3 heterointerfaces are defined as $E^{AlGaO/AlO}_{Ga\ 3s}$ and $E^{AlGaO/AlO}_{Al\ 2p}$, respectively. The bandgaps of α-Al_2O_3 and α-$(Al_xGa_{1-x})_2O_3$ are represented as E^{AlO}_g and E^{AlGaO}_g. The Al 2p and Ga 3s core levels and the valance band spectra for α-Al_2O_3 and α-$(Al_xGa_{1-x})_2O_3$ films and α-$(Al_xGa_{1-x})_2O_3$/α-Al_2O_3 heterojunctions are shown as exemplarily in Figure 13, for 50% Al compositions. The core level positions are determined by fitting with Gaussian and Lorentzian line shapes after applying the Shirley background subtraction and the valance band onsets are determined by linear extrapolation of the leading edge to the background. By using equation (1), the valance band offsets of 0.03, 0.10 and 0.27 eV were determined at α-$(Al_xGa_{1-x})_2O_3$/α-Al_2O_3 interfaces with Al compositions of 78%, 50% and 0%. The corresponding conduction band offsets of 0.90, 2.26, and 3.13 eV were calculated from equation (2) by using the valance band offsets and the bandgaps of α-$(Al_xGa_{1-x})_2O_3$ and α-Al_2O_3. The measured core-level binding energies, the valance and conduction band offsets at α-$(Al_xGa_{1-x})_2O_3$/α-Al_2O_3 interfaces with Al compositions of 78%, 50% and 0% are summarized in Table 3.

Finally, the evolution of the band alignments between α-Al_2O_3 and α-$(Al_xGa_{1-x})_2O_3$ grown on m-plane sapphire substrates with Al compositions of 78%, 50% and 0% are plotted in Figure 14. The α-$(Al_xGa_{1-x})_2O_3$/α-Al_2O_3 interfaces show type-I (straddling) band alignment for all the investigated Al compositions which is consistent with the theoretical DFT predictions for α-Ga_2O_3/α-Al_2O_3 interfaces [8,55]. Previously, type I band discontinuity at mist-CVD grown α-$(Al_xGa_{1-x})_2O_3$/α-Ga_2O_3 interfaces on c-plane sapphire substrates was also reported [42]. As the Al composition increases, both valance and conduction band offsets between α-Al_2O_3 and α-$(Al_xGa_{1-x})_2O_3$ are found to decrease as shown in Figure 14. The valance (ΔE_v) and conduction (ΔE_c) band offsets of 0.27 eV and 3.13 eV were determined at α-Ga_2O_3/α-Al_2O_3 interface, which closely match with theoretical calculations (ΔE_v = 0.24 eV and ΔE_v = 3.24 eV) [8]. Since O 2p localized states dominate the valance band, much weaker variations in the valance band offsets are observed as compared to the variations in the conduction band offsets. Such weaker variation in the valance band offsets are predicted by theory [8,55] and was also reported by previous experimental studies on both α- [42] and β- [12] phase $(Al_xGa_{1-x})_2O_3$/Ga_2O_3 heterointerfaces.

IV. Conclusion

In summary, the epitaxial growth of high-quality phase pure α-$(Al_xGa_{1-x})_2O_3$ thin films and α-$(Al_xGa_{1-x})_2O_3$/α-Al_2O_3 SL structures on m-plane sapphire substrates are successfully demonstrated by MOCVD. The structural, physical, and surface morphological properties such as the Al incorporation, strain characteristics, RC FWHMs, surface RMS roughness, interfacial abruptness, and alloy homogeneity of α-Ga_2O_3 and α-$(Al_xGa_{1-x})_2O_3$ alloys were investigated by comprehensive characterization. XRD and atomic resolution STEM images for different Al composition samples reveal high crystalline quality of the films with sharp interfaces and homogenous Al distribution. The coherent growth of α-$(Al_xGa_{1-x})_2O_3$/α-Al_2O_3 SL structures were also confirmed by XRD,

STEM and RSM mapping. Although smooth surface morphologies were observed, lower Al composition samples exhibit relatively higher surface RMS roughness due to the increase in the lattice mismatch between the substrate and epilayer. The epitaxial stabilization of phase pure α-Ga_2O_3 was observed for lower growth temperature (650°C). Higher chamber pressure led to lower Al incorporation in α-$(Al_xGa_{1-x})_2O_3$ films due to the increase in the gas phase reaction of precursors. By varying the Al compositions from 0% to 100%, the bandgap energies from 5.41 eV to 8.81 eV with a bowing parameter of 2.16 eV were extracted by XPS measurement. The determined band offsets reveal the formation of type-I (straddling) band alignment at α-$(Al_xGa_{1-x})_2O_3$/α-Al_2O_3 heterointerfaces. Both valance and conduction band offsets increase with the decrease of the Al compositions in α-$(Al_xGa_{1-x})_2O_3$ films. The valance and conduction band offsets of 0.27 eV and 3.13 eV were determined between α-Ga_2O_3 and α-Al_2O_3, respectively. The results from this study on the epitaxial growth of ultrawide bandgap α-Ga_2O_3 and α-$(Al_xGa_{1-x})_2O_3$ alloys and the band offset at α-$(Al_xGa_{1-x})_2O_3$/α-Al_2O_3 will contribute in designing and fabricating future high power heterostructure based electronic and optoelectronic devices.

Supplementary Online Material

See the supplementary material for the FESEM images of α-$(Al_xGa_{1-x})_2O_3$ films with different Al compositions, AFM images for α-$(Al_{0.50}Ga_{0.50})_2O_3$ films grown with different thicknesses, the XPS survey spectra, schematic of the samples grown for band offset measurements and the summary of the Al compositions calculated by using Ga 3s, Al 2p and Al 2s core level spectra from XPS.

Acknowledgements

The authors acknowledge the Air Force Office of Scientific Research FA9550-18-1-0479 (AFOSR, Dr. Ali Sayir) for financial support. The authors also acknowledge the National Science Foundation (Grant No. 1810041, No. 2019753) and Semiconductor Research Corporation (SRC) under the Task ID GRC 3007.001 for partial support. Electron microscopy was performed at the Center for Electron Microscopy and Analysis (CEMAS) at The Ohio State University.

Data Availability Statements

The data that support the findings of this study are available from the corresponding author upon reasonable request.

References

1. R. Roy, V. G. Hill, and E. F. Osborn, J. Am. Chem. Soc. 74, 719 (1952).
2. D. Shinohara and S. Fujita, Jpn. J. Appl. Phys. 47, 7311 (2008).
3. M. Higashiwaki and G. H. Jessen, Appl. Phys. Lett. 112, 060401 (2018).
4. A. Kuramata, K. Koshi, S. Watanabe, Y. Yamaoka, T. Masui, and S. Yamakoshi, Jpn. J. Appl. Phys., Part 1 55, 1202A2 (2016).
5. Z. Feng, A. F. M. A. U. Bhuiyan, M. R. Karim, and H. Zhao, Appl. Phys. Lett. 114, 250601 (2019).
6. G. Seryogin, F. Alema, N. Valente, H. Fu, E. Steinbrunner, A. T. Neal, S. Mou, A. Fine, and A. Osinsky, Appl. Phys. Lett. 117, 262101 (2020).
7. Z. Feng, A F M A. U. Bhuiyan, Z. Xia, W. Moore, Z. Chen, J. F. McGlone, D. R. Daughton, A. R. Arehart, S. A. Ringel, S. Rajan, and H. Zhao, Phys. Status Solidi RPL. 14, 2000145 (2020).
8. H. Peelaers, J. B. Varley, J. S. Speck, and C. G. Van de Walle, Appl. Phys. Lett. 112, 242101 (2018).
9. A F M A. U. Bhuiyan, Z. Feng, J. M. Johnson, Z. Chen, H.-L. Huang, J. Hwang, and H. Zhao, Appl. Phys. Lett. 115, 120602 (2019).
10. A F M A. U. Bhuiyan, Z. Feng, J. M. Johnson, H.-L. Huang, J. Sarker, M. Zhu, M. R. Karim, B. Mazumder, J. Hwang, and H. Zhao, APL Mater. 8, 031104 (2020).
11. A F M A. U. Bhuiyan, Z. Feng, J. M. Johnson, H.-L. Huang, J. Hwang, and H. Zhao, Cryst. Growth Des. 20, 6722 (2020).
12. A F M A. U. Bhuiyan, Z. Feng, J. M. Johnson, H.-L. Huang, J. Hwang, and H. Zhao, Appl. Phys. Lett. 117, 252105 (2020).

13. A F M A. U. Bhuiyan, Z. Feng, J. M. Johnson, H.-L. Huang, J. Hwang, and H. Zhao, Appl. Phys. Lett. 117, 142107 (2020).
14. A F M A. U. Bhuiyan, Z. Feng, L. Meng, H. Zhao, J. Mater. Res. MOCVD growth of (010) β-$(Al_xGa_{1-x})_2O_3$ thin films (2021). https://doi.org/10.1557/s43578-021-00354-8
15. T. Oshima, T. Okuno, N. Arai, Y. Kobayashi, and S. Fujita, Jpn. J. Appl. Phys. Part 1 48, 070202 (2009).
16. S. W. Kaun, F. Wu, and J. S. Speck, J. Vac. Sci. Technol. A 33, 041508 (2015).
17. P. Vogt, A. Mauze, F. Wu, B. Bonef, and J. S. Speck, Appl. Phys. Express 11, 115503 (2018).
18. S. Krishnamoorthy, Z. Xia, C. Joishi, Y. Zhang, J. McGlone, J. Johnson, M. Brenner, A. R. Arehart, J. Hwang, S. Lodha, and S. Rajan, Appl. Phys. Lett. 111, 023502 (2017).
19. P. Ranga, A. Bhattacharyya, A. Rishinaramangalam, Y. K Ooi, M. A. Scarpulla, D. Feezell and S. Krishnamoorthy, Appl. Phys. Express 13, 045501 (2020).
20. Y. Zhang, A. Neal, Z. Xia, C. Joishi, J. M. Johnson, Y. Zheng, S. Bajaj, M. Brenner, D. Dorsey, K. Chabak, G. Jessen, J. Hwang, S. Mou, J. P. Heremans, and S. Rajan, Appl. Phys. Lett. 112, 173502 (2018).
21. N. K. Kalarickal, Z. Feng, A F M A. U. Bhuiyan, Z. Xia, J. F. McGlone, W. Moore, A. R. Arehart, S. A. Ringel, H. Zhao, and S. Rajan, IEEE Transaction on Electron Devices, 68, 29-35 (2021).
22. A F M A. U. Bhuiyan, Z. Feng, J. M. Johnson, H.-L. Huang, J. Sarker, M. Zhu, M. R. Karim, B. Mazumder, J. Hwang, and H. Zhao, APL Materials 8 (8), 089102 (2020).
23. J. M. Johnson, H.-L. Huang, M. Wang, S. Mu, J. B. Varley, A. F. M. A. U. Bhuiyan, Z. Feng, N. K. Kalarickal, S. Rajan, H. Zhao, C. G. Van de Walle, and J. Hwang, APL Materials 9, 051103 (2021).
24. S. Mu, H. Peelaers, Y. Zhang, M. Wang, and C. G. Van de Walle, Appl. Phys. Lett. 117, 252104 (2020).
25. T. Kawaharamura, G. T. Dang, and M. Furuta, Jpn. J. Appl. Phys. 51, 040207 (2012).
26. R. Schewski, G. Wagner, M. Baldini, D. Gogova, Z. Galazka, T. Schulz, T. Remmele, T. Markurt, H. von Wenckstern, M. Grundmann, O. Bierwagen, P. Vogt, and M. Albrecht, Appl. Phys. Express. 8, 011101 (2015).
27. K. Akaiwa, and S. Fujita, Jpn. J. Appl. Phys. 51, 070203 (2012).
28. K. Akaiwa, K. Ota, T. Sekiyama, T. Abe, T. Shinohe, and K. Ichino, Phys. status solidi. 217, 1900632 (2020).
29. Y. Oshima, E. G. Víllora, and K. Shimamura, Appl. Phys. Express. 8, 055501 (2015).
30. M. Kracht, A. Karg, M. Feneberg, J. Bläsing, J. Schörmann, R. Goldhahn, and M. Eickhoff, Phys. Rev. Appl. 10, 024047 (2018).
31. K. Kaneko, H. Kawanowa, H. Ito, and S. Fujita, Jpn. J. Appl. Phys. 51, 020201 (2012).
32. R. Jinno, C. S. Chang, T. Onuma, Y. Cho, S.-T. Ho, D. Rowe, M. C. Cao, K. Lee, V. Protasenko, D. G. Schlom, D. A. Muller, H. G. Xing, D. Jena, Sci. Adv. 7, (2021).

33. D.-W. Jeon, H. Son, J. Hwang, A. Y. Polyakov, N. B. Smirnov, I. V. Shchemerov, A. V. Chernykh, A. I. Kochkova, S. J. Pearton, and I.-H. Lee, APL Mater. 6, 121110 (2018).
34. M. Lorenz, S. Hohenberger, E. Rose, and M. Grundmann, Appl. Phys. Lett. 113, 231902 (2018).
35. G. T. Dang, T. Yasuoka, Y. Tagashira, T. Tadokoro, W. Theiss, and T. Kawaharamura, Appl. Phys. Lett. 113, 062102 (2018).
36. Z. Cheng, M. Hanke, P. Vogt, O. Bierwagen, and A. Trampert, Appl. Phys. Lett. 111, 162104 (2017).
37. K. Kaneko, T. Nomura, and S. Fujita, Phys. Status Solidi C 7, 2467 (2010).
38. N. Suzuki, K. Kaneko, and S. Fujita, J. Cryst. Growth 364, 30 (2013).
39. A. K. Harman, S. Ninomiya, and S. Adachi, J. Appl. Phys. 76, 8032 (1994).
40. G. T. Dang, T. Kawaharamura, M. Furuta, and M. W. Allen, IEEE Trans. Electron Devices 62, 3640 (2015).
41. H. Ito, K. Kaneko, and S. Fujita, Jpn. J. Appl. Phys. 51 100207 (2012).
42. T. Uchida, R. Jinno, S. Takemoto, K. Kaneko, and S. Fujita, Jpn. J. Appl. Phys. 57, 040314 (2018).
43. R. Kumaran, T. Tiedje, S. E. Webster, S. Penson, and W. Li, Opt. Lett. 35, 3793 (2010).
44. T. Maeda, M. Yoshimoto, T. Ohnishi, G. H. Lee, and H. Koinuma, J. Cryst. Growth 177, 95 (1997).
45. D. Shiojiri, R. Yamaguchi, S. Kaneko, A. Matsuda, and M. Yoshimoto, J. Ceram. Soc. Japan. 121, 467 (2013).
46. K. Akaiwa, K. Kaneko, K. Ichino, S. Fujita, Jpn. J. Appl. Phys. 55, 1202BA (2016).
47. R. Jinno, T. Uchida, K. Kaneko, and S. Fujita, Appl. Phys. Express 9, 071101 (2016).
48. G. Pezzotti and W. Zhu, Phys. Chem. Chem. Phys. 17, 2608 (2015).
49. W. Zhu and G. Pezzotti,, J. Raman Spectrosc. 42, 2015 (2011).
50. R. Jinno, K. Kaneko, and S. Fujita, Jpn. J. Appl. Phys. 60, SBBD13 (2021).
51. M. T. Nichols, W. Li, D. Pei, G. A. Antonelli, Q. Lin, S. Banna, Y. Nishi, and J. L. Shohet, J. Appl. Phys. 115, 094105 (2014).
52. B. W. Krueger, C. S. Dandeneau, E. M. Nelson, S. T. Dunham, F. S. Ohuchi, and M. A. Olmstead, J. Am. Ceram. Soc. 99, 2467 (2016).
53. H. Peelaers, J. B. Varley, J. S. Speck, and C. G. Van de Walle, Appl. Phys. Lett. 115, 159901 (2019).
54. E. A. Kraut, R. W. Grant, J. R. Waldrop, and S. P. Kowalczyk, Phys. Rev. Lett. 44, 1620 (1980).
55. T. Wang, W. Li, C. Ni, and A. Janotti, Phys. Rev. Appl. 10, 011003 (2018).

Table Captions

Table 1. Summary of α-$(Al_xGa_{1-x})_2O_3$ films grown with different [TMAl]/[TEGa+TMAl] molar flow rate ratio ranging from 0% to 100%. The corresponding TEGa and TMAl molar flow rates, growth temperature, Al compositions, film thicknesses and growth rates are included. All films were grown at chamber pressure of 20 torr.

Table 2. Comparison between the Al compositions extracted from XRD and XPS measurements, showing good agreement. The corresponding energy bandgaps measured by XPS are also included.

Table 3. Summary of the valance and conduction band offsets at α-$(Al_xGa_{1-x})_2O_3$/α-Al_2O_3 interfaces, estimated by using valance band maximum, Ga 3s, and Al 2p core levels from XPS measurements.

Figure Captions

Figure 1. (a) XRD ω-2θ scan profiles for the $(30\bar{3}0)$ reflections of α-$(Al_xGa_{1-x})_2O_3$ films grown on m-plane sapphire substrates. Red arrows indicate the peak positions of α-$(Al_xGa_{1-x})_2O_3$ films for Al compositions ranging from 0% to 100%. (b) XRD Φ-scan profiles of the asymmetric $(22\bar{4}0)$ peak of $(30\bar{3}0)$ reflections of α-$(Al_xGa_{1-x})_2O_3$ films for Al compositions of 78% and 0%. (c) XRD rocking curve FWHMs of α-$(Al_xGa_{1-x})_2O_3$ films as a function of Al compositions.

Figure 2. X-ray asymmetrical reciprocal space mapping (RSMs) around $(22\bar{4}0)$ reflections of α-$(Al_xGa_{1-x})_2O_3$ films grown with Al compositions of (a) 0%, (b) x= 15%, (c) x= 50%, and (d) 78%.

Figure 3. The surface AFM images (5μm x 5μm scan area) of α-$(Al_xGa_{1-x})_2O_3$ films grown with different Al compositions.

Figure 4. Room-temperature Raman spectra of α-$(Al_xGa_{1-x})_2O_3$ films grown by varying the Al compositions from 0% to 100%. The excitation wavelength was 514 nm.

Figure 5. XRD ω-2θ scan spectra of (a) α-Ga_2O_3 films grown at (i) 880°C and (ii) 650°C with the same chamber pressure of 20 torr. (b) α-$(Al_xGa_{1-x})_2O_3$ films grown at the same growth temperature (880°C) and [TMAl]/[TMAl+TEGa] molar flow ratio (49.24%) with different chamber pressures of (i) 80 and (ii) 20 torr.

Figure 6. Asymmetrical reciprocal space mapping (RSMs) around $(22\bar{4}0)$ reflections of α-$(Al_{0.50}Ga_{0.50})_2O_3$ films grown with (a) 75 nm, (b) 30 nm, (c) 15 nm, and (d) 7.5 nm thicknesses.

Figure 7. Atomic resolution cross-sectional HAADF-STEM images of (a, b) α-Ga_2O_3 and α-$(Al_xGa_{1-x})_2O_3$ films with (c, d) 50% and (e, f) 78% Al compositions with (a, c, e) 5 nm and (b, d, f) 2 nm scale. The white dashed lines represent the substrate-epilayer interfaces. The HAADF-STEM images were taken from the <0001> (α-Ga_2O_3 films) and $<12\bar{3}\bar{1}>$ (α-$(Al_xGa_{1-x})_2O_3$ films) zone axes.

Figure 8. STEM-EDS mapping for (a-d) α-Ga_2O_3 and α-$(Al_xGa_{1-x})_2O_3$ films with (e-h) 50% and (i-l) 78% Al compositions. (a) HAADF images for (a) α-Ga_2O_3 and α-$(Al_xGa_{1-x})_2O_3$ films with (e) 50% and (i) 78% Al compositions with their corresponding (b, f, j) Ga and (c, g, k) Al EDS maps and (d, h, l) atomic fraction elemental profile as indicated by the orange arrows in (a, e, i).

Figure 9. (a) Schematic of 8 period α-$(Al_xGa_{1-x})_2O_3$/α-Al_2O_3 superlattice structure grown with 78% Al composition in α-$(Al_xGa_{1-x})_2O_3$ layers; (b) XRD ω-2θ scan spectrum of the $(30\bar{3}0)$ reflection; and (c) x-ray asymmetrical reciprocal space mapping (RSMs) around $(22\bar{4}0)$ reflection of the SL structure with 78% Al composition.

Figure 10. Atomic resolution cross-sectional HAADF-STEM images of 8 period α-$(Al_xGa_{1-x})_2O_3$/α-Al_2O_3 superlattice structures grown with (a, e) 78% and (b, f) 50% Al compositions. In addition, 8 period α-$(Al_xGa_{1-x})_2O_3$/α-Ga_2O_3 SL structures with (c, g) 50% and (d, h) 17% Al compositions are also shown with (a,b,c,d) 50 nm and (e,f,g,h) 2 nm scale. Corresponding layer thicknesses are included for different structures. The white dashed lines represent the substrate-epilayer interfaces. The HAADF-STEM images of α-$(Al_xGa_{1-x})_2O_3$/α-Al_2O_3 superlattice structures with 78% and 50% Al compositions were taken from $<24\bar{6}1>$ and <0001> zone axes, respectively. And both α-$(Al_xGa_{1-x})_2O_3$/α-Ga_2O_3 SL structures with 50% and 17% Al compositions were viewed along $<12\bar{3}\bar{1}>$ zone axes.

Figure 11. STEM-EDS mapping for α-$(Al_xGa_{1-x})_2O_3$/α-Al_2O_3 superlattice structures grown with (a-d) 78% and (e-h) 50% Al compositions and α-$(Al_xGa_{1-x})_2O_3$/α-Ga_2O_3 SL structures with (i-l) 50% and (m-p) 17% Al compositions. (a,e,i,m) HAADF images with their corresponding (b, f, j,n) Ga and (c, g, k,o) Al EDS maps and (d, h, l, p) atomic fraction elemental profile as indicated by the orange arrows in (a, e, i, m).

Figure 12. The bandgap energies of (a) α-Ga_2O_3, (b) α-$(Al_xGa_{1-x})_2O_3$ films with 50% Al composition and (c) α-Al_2O_3 films determined by calculating the energy difference between Ga $2p_{3/2}$ or O 1s core level peak and the onset of energy loss spectrum. The inset figures represent the zoomed view of the background region of the Ga $2p_{3/2}$ and O 1s core levels. (d) The bandgap energies of α-$(Al_xGa_{1-x})_2O_3$ films as a function of Al compositions, showing a good agreement with the theoretically predicted bandgap values [8].

Figure 13. Al 2p and Ga 3s core-levels and valence band (VB) spectra from 50 nm thick (a) α-Al_2O_3 film (b) α-$(Al_xGa_{1-x})_2O_3$ film and (c) α-$(Al_xGa_{1-x})_2O_3$/α-Al_2O_3 interface with x = 0.50. Data are shown as blue open circles and the fitted curves are represented as black dashed lines for Ga 3s and Al 2p core-levels. Red solid straight lines represent the linear fitting of VB spectra of α-Al_2O_3 and α-$(Al_xGa_{1-x})_2O_3$ films.

Figure 14. Summary of the valance and conduction band offsets at α-Al_2O_3/α-$(Al_xGa_{1-x})_2O_3$ interfaces with Al composition of 78%, 50% and 0%, The corresponding bandgap energies of α-$(Al_xGa_{1-x})_2O_3$ films for different Al compositions are also included.

Table 1.

Summary of α-$(Al_xGa_{1-x})_2O_3$ films grown with different [TMAl]/[TEGa+TMAl] molar flow rate ratio ranging from 0% to 100%. The corresponding TEGa and TMAl molar flow rates, growth temperature, Al compositions, film thicknesses and growth rates are included. All films are grown at chamber pressure of 20 torr.

Sample Id	TEGa molar flow rate (μmole min^{-1})	TMAl molar flow rate (μmole min^{-1})	[TMAl]/[TMAl+TEGa] (%)	Growth Temperature (°C)	Al composition (%)	$(Al_xGa_{1-x})_2O_3$ film thickness (nm)	Growth rates (μm/hr)
#1	19.12	0	0	650	0	85	0.51
#2	19.12	0.76	3.82	880	15	88	0.53
#3	19.12	1.06	5.25	880	21	89	0.53
#4	19.12	1.50	7.27	880	28	92	0.55
#5	19.12	2.21	10.36	880	36	110	0.66
#6	19.12	4.22	18.08	880	50	150	0.90
#7	19.12	6.62	25.72	880	58	128	0.96
#8	14.35	7.73	35.00	880	68	156	0.94
#9	11.95	9.76	44.96	880	75	173	1.04
#10	11.95	11.59	49.24	880	78	200	1.33
#11	0	6.62	100.00	880	100	135	0.27

Table 2.

Comparison between the Al compositions estimated from XRD and XPS measurements, showing a good agreement. The corresponding bandgaps measured by XPS are also included.

Sample Id	[TMAl]/[TMAl+ TEGa] (%)	Al composition (XRD) (%)	Al composition (XPS) (%)	Bandgap energy (eV) (± 0.15 eV)
#1	0	0	0	5.41
#4	7.27	28	30	5.99
#6	18.08	50	50	6.45
#8	35.00	68	65	7.30
#10	49.24	78	75	7.88
#11	100.00	100	100	8.81

Table 3.

Summary of the valance and conduction band offsets at α-$(Al_xGa_{1-x})_2O_3$/α-Al_2O_3 interfaces, estimated by using valance band maximum, Ga 3s, and Al 2p core levels from XPS measurement.

Al composition	**Bandgap energy (eV) (± 0.15 eV)**	**($E^{AlO}_{Al\ 2p}$ - E^{AlO}_{VBM}) (eV) (± 0.04 eV)**	**($E^{AlGaO}_{Ga\ 3s}$ - E^{AlGaO}_{VBM}) (eV) (± 0.04 eV)**	**($E^{AlGaO/GaO}_{Ga\ 3s}$ - $E^{AlGaO/GaO}_{Al\ 2p}$) (eV) (± 0.02 eV)**	**ΔE_v (eV) (± 0.06 eV)**	**ΔE_c (eV) (± 0.22 eV)**
100%	8.81	70.75				
78%	7.88		157.47	86.68	0.03	0.90
50%	6.45		157.36	86.51	0.10	2.26
0%	5.41		157.31	86.29	0.27	3.13

Figure 1

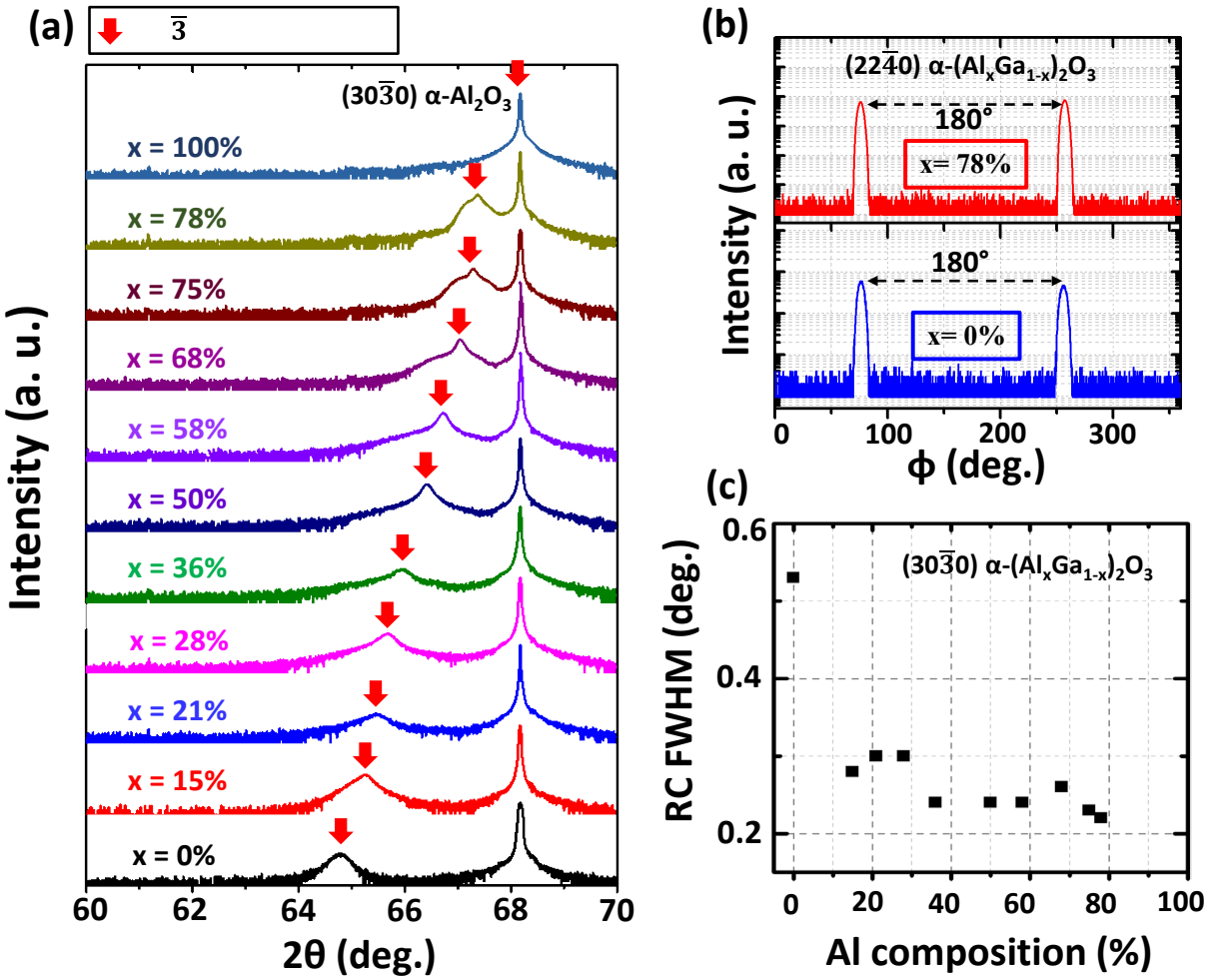

Figure 1. (a) XRD ω-2θ scan profiles for the (30$\bar{3}$0) reflections of α-$(Al_xGa_{1-x})_2O_3$ films grown on m-plane sapphire substrates. Red arrows indicate the peak positions of α-$(Al_xGa_{1-x})_2O_3$ films for Al compositions ranging from 0% to 100%. (b) XRD Φ-scan profiles of the asymmetric (22$\bar{4}$0) peak of (30$\bar{3}$0) reflections of α-$(Al_xGa_{1-x})_2O_3$ films for Al compositions of 78% and 0%. (c) XRD rocking curve FWHMs of α-$(Al_xGa_{1-x})_2O_3$ films as a function of Al compositions.

Figure 2

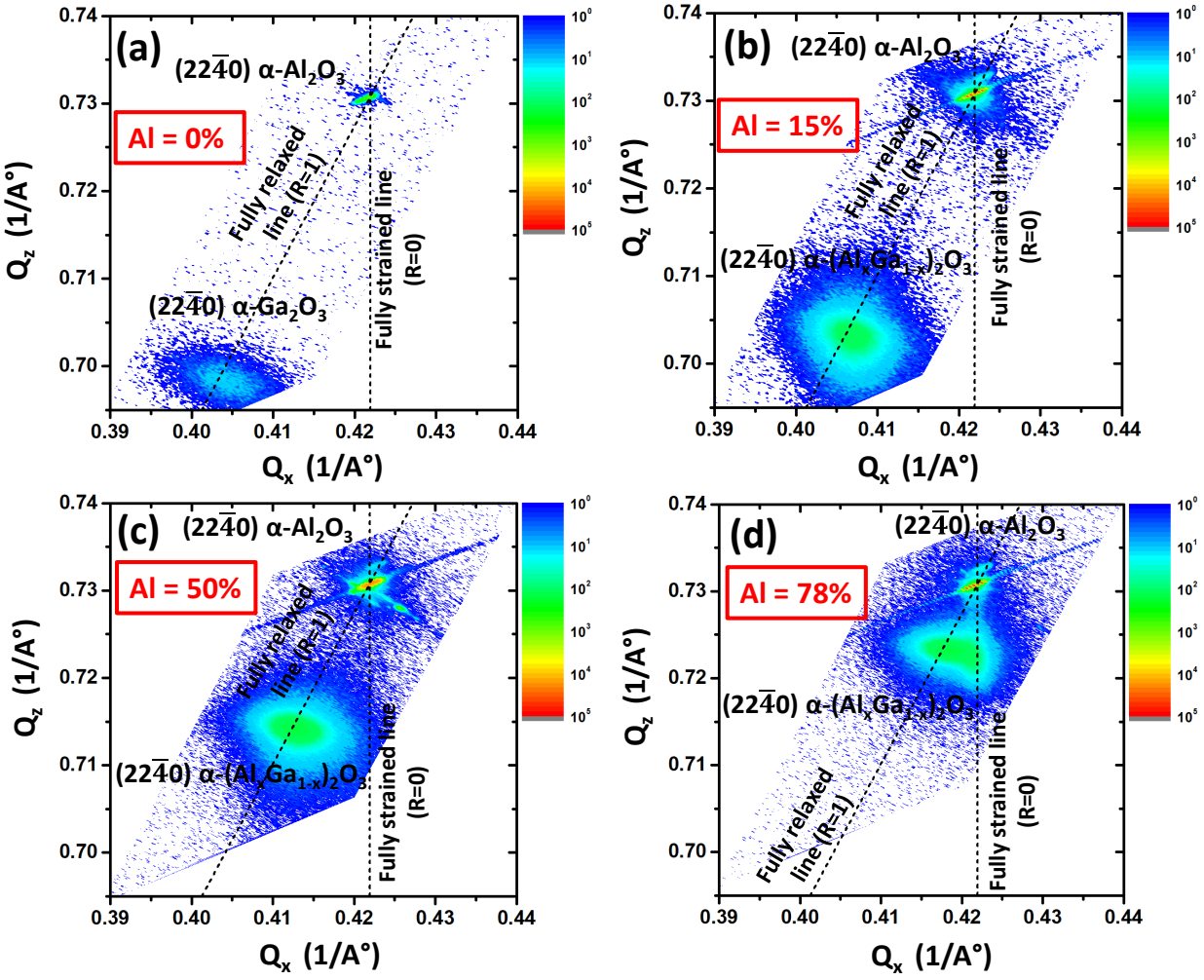

Figure 2. X-ray asymmetrical reciprocal space mapping (RSMs) around (22$\bar{4}$0) reflections of α-$(Al_xGa_{1-x})_2O_3$ films grown with Al compositions of (a) 0%, (b) x= 15%, (c) x= 50%, and (d) 78%.

Figure 3

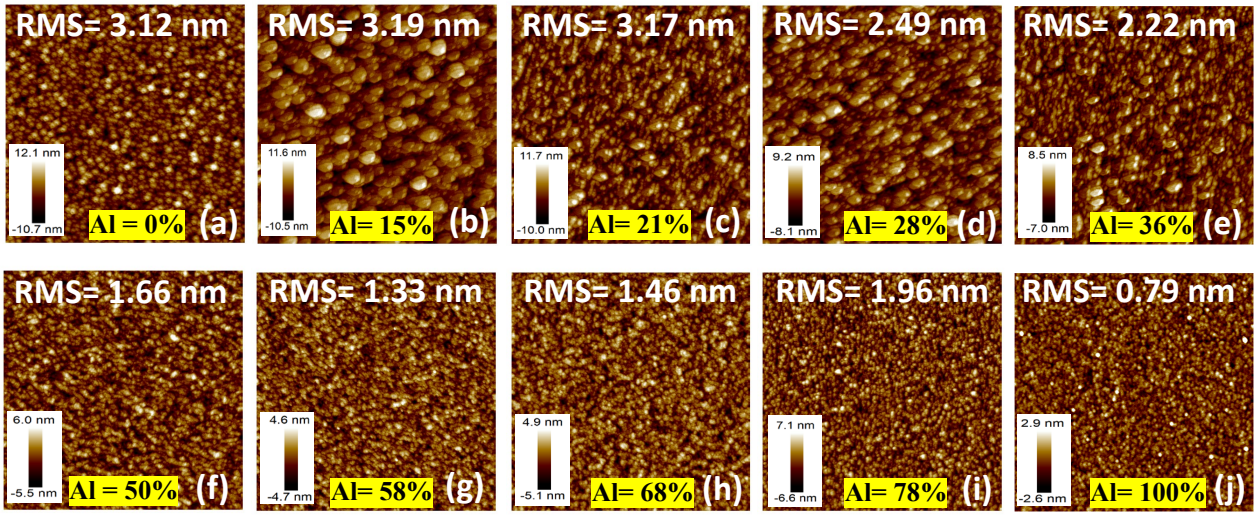

Figure 3. The surface AFM images (5μm x 5μm scan area) of α-$(Al_xGa_{1-x})_2O_3$ films grown with different Al compositions.

Figure 4

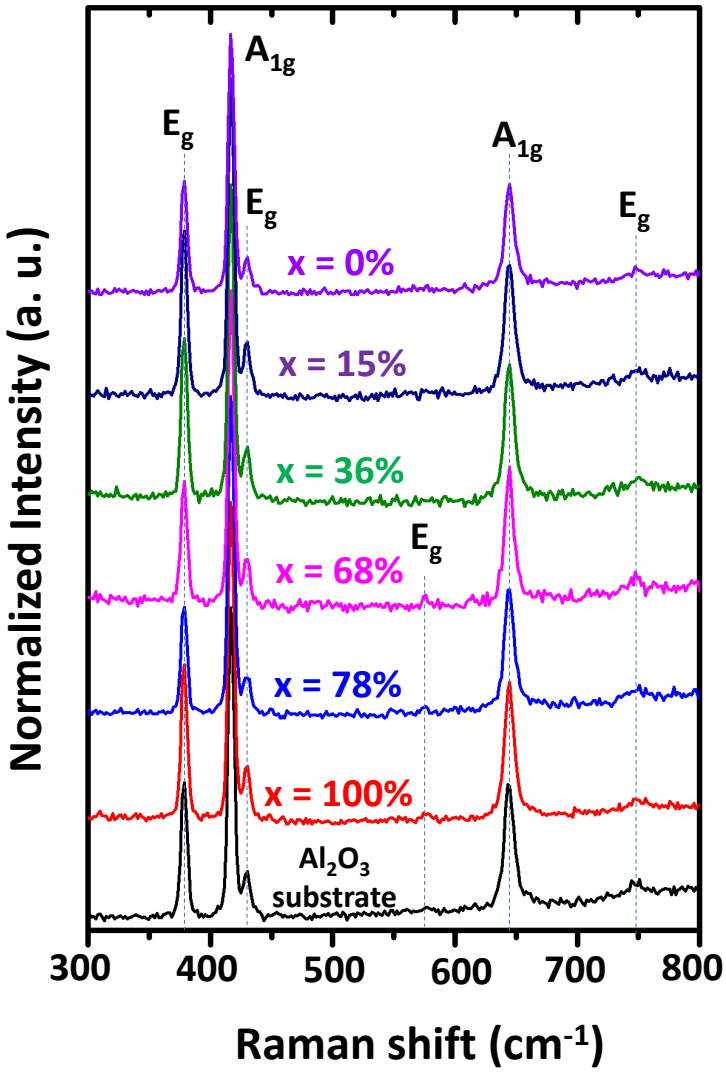

Figure 4. Room-temperature Raman spectra of α-$(Al_xGa_{1-x})_2O_3$ films grown by varying the Al compositions from 0% to 100%. The excitation wavelength was 514 nm.

Figure 5

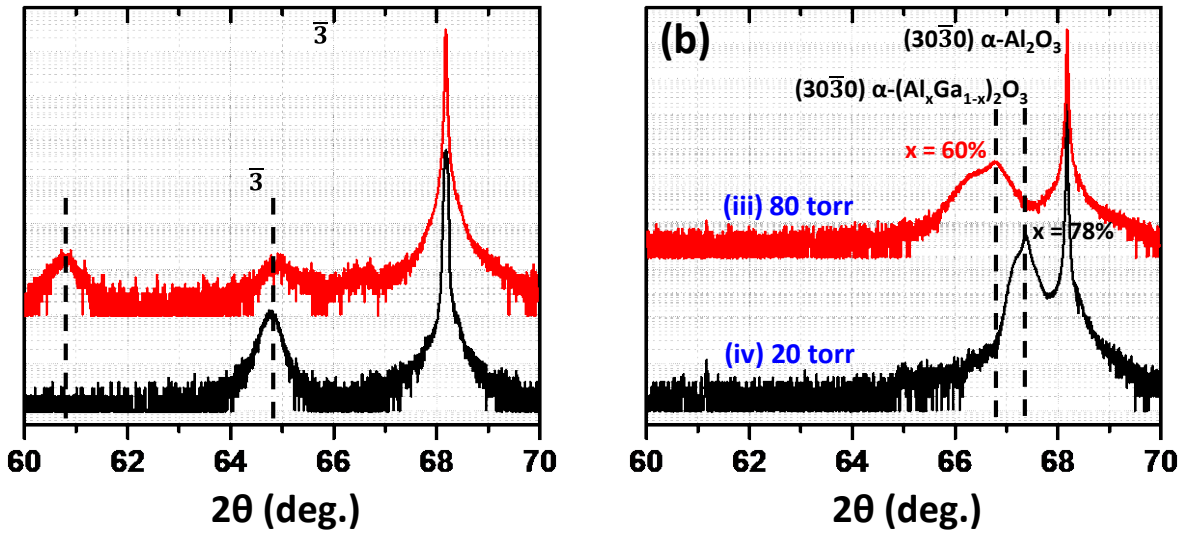

Figure 5. XRD ω-2θ scan spectra of (a) α-Ga_2O_3 films grown at (i) 880°C and (ii) 650°C with same chamber pressure of 20 torr. (b) α-$(Al_xGa_{1-x})_2O_3$ films grown at same growth temperature (880°C) and [TMAl]/[TMAl+TEGa] molar flow ratio (49.24%) with different chamber pressures of (iii) 80 and (iv) 20 torr.

Figure 6

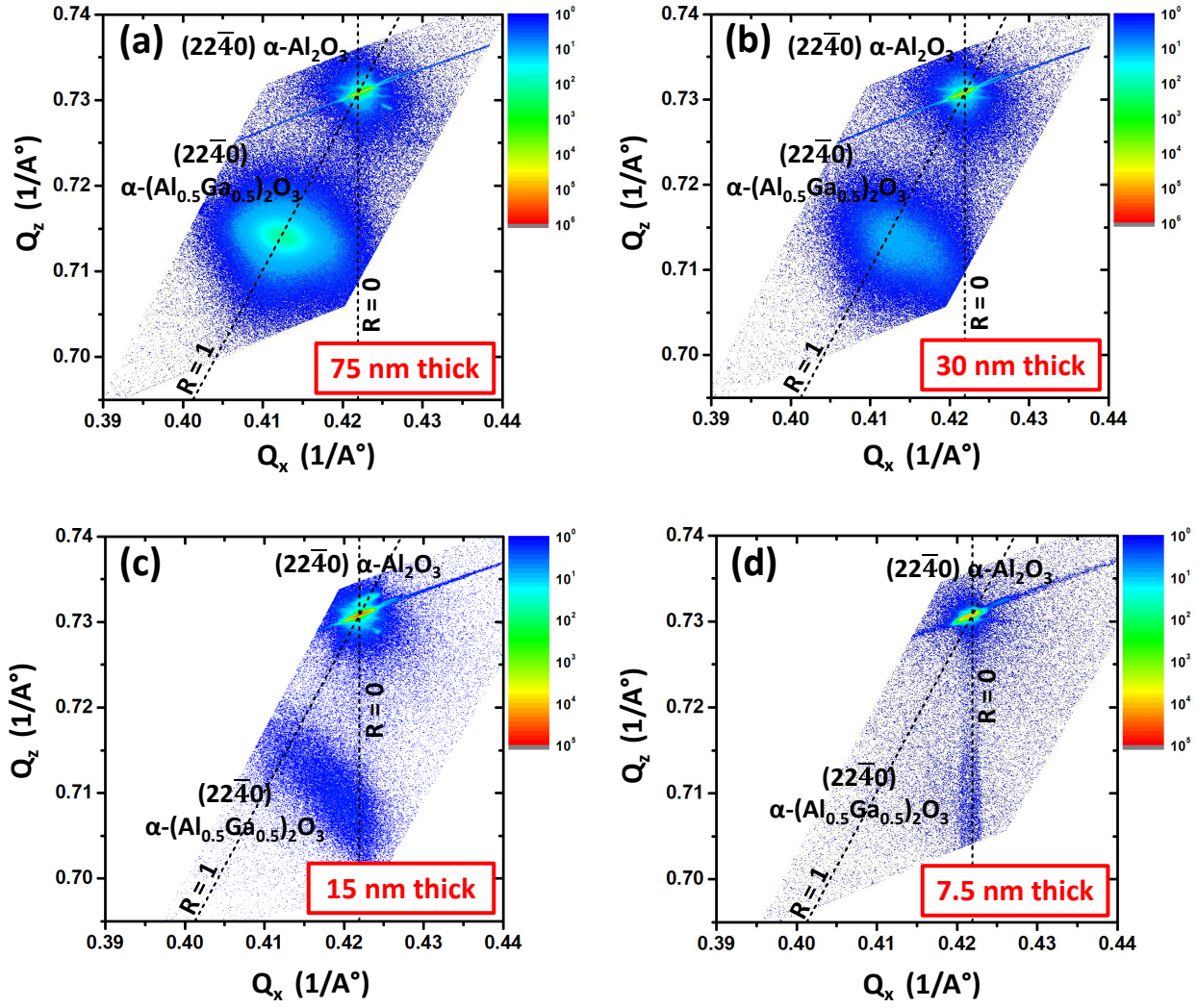

Figure 6. Asymmetrical reciprocal space mapping (RSMs) around (22$\bar{4}$0) reflections of α-$(Al_{0.50}Ga_{0.50})_2O_3$ films grown with (a) 75 nm, (b) 30 nm, (c) 15 nm, and (d) 7.5 nm thicknesses.

Figure 7

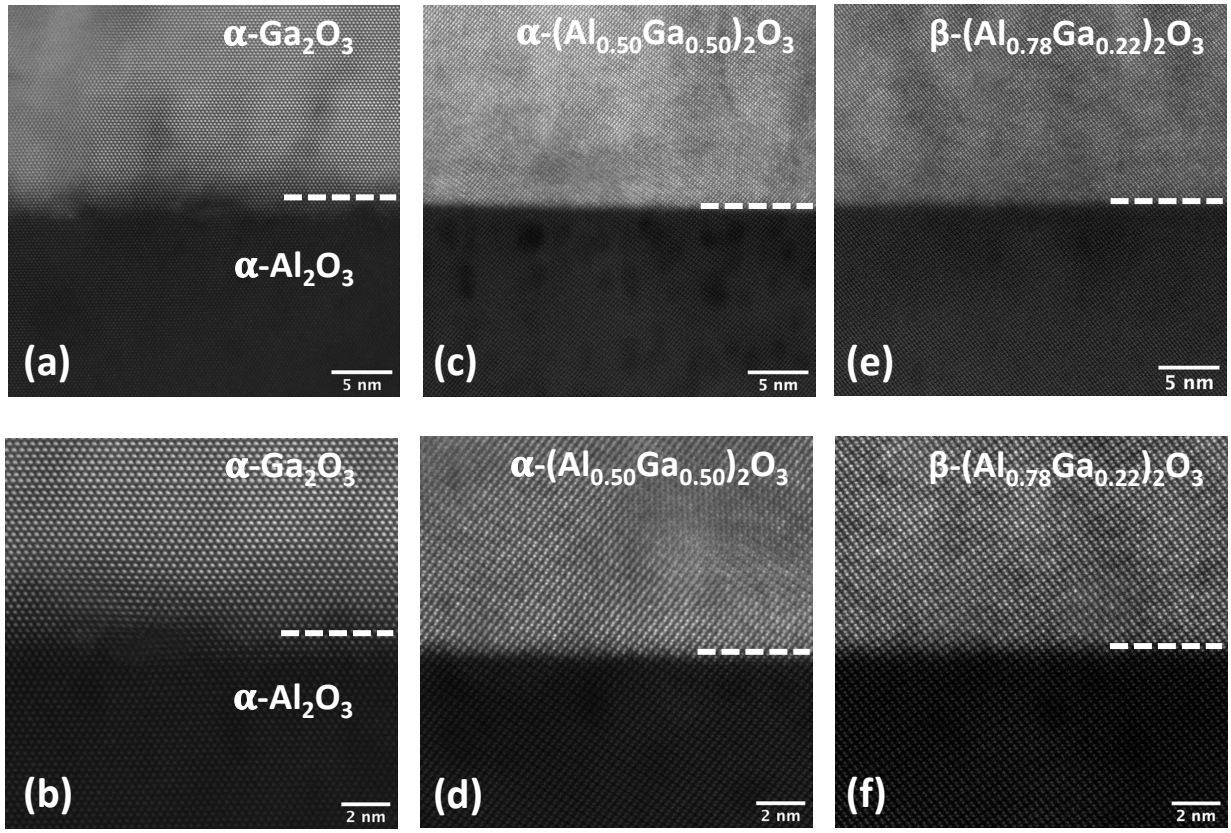

Figure 7. Atomic resolution cross-sectional HAADF-STEM images of (a, b) α-Ga_2O_3 and α-$(Al_xGa_{1-x})_2O_3$ films with (c, d) 50% and (e, f) 78% Al compositions on (a, c, e) 5 nm and (b, d, f) 2 nm scale. The white dashed lines represent the substrate-epilayer interfaces. The HAADF-STEM images were taken from the <0001> (α-Ga_2O_3 films) and <$12\bar{3}\bar{1}$> (α-$(Al_xGa_{1-x})_2O_3$ films) zone axes.

Figure 8

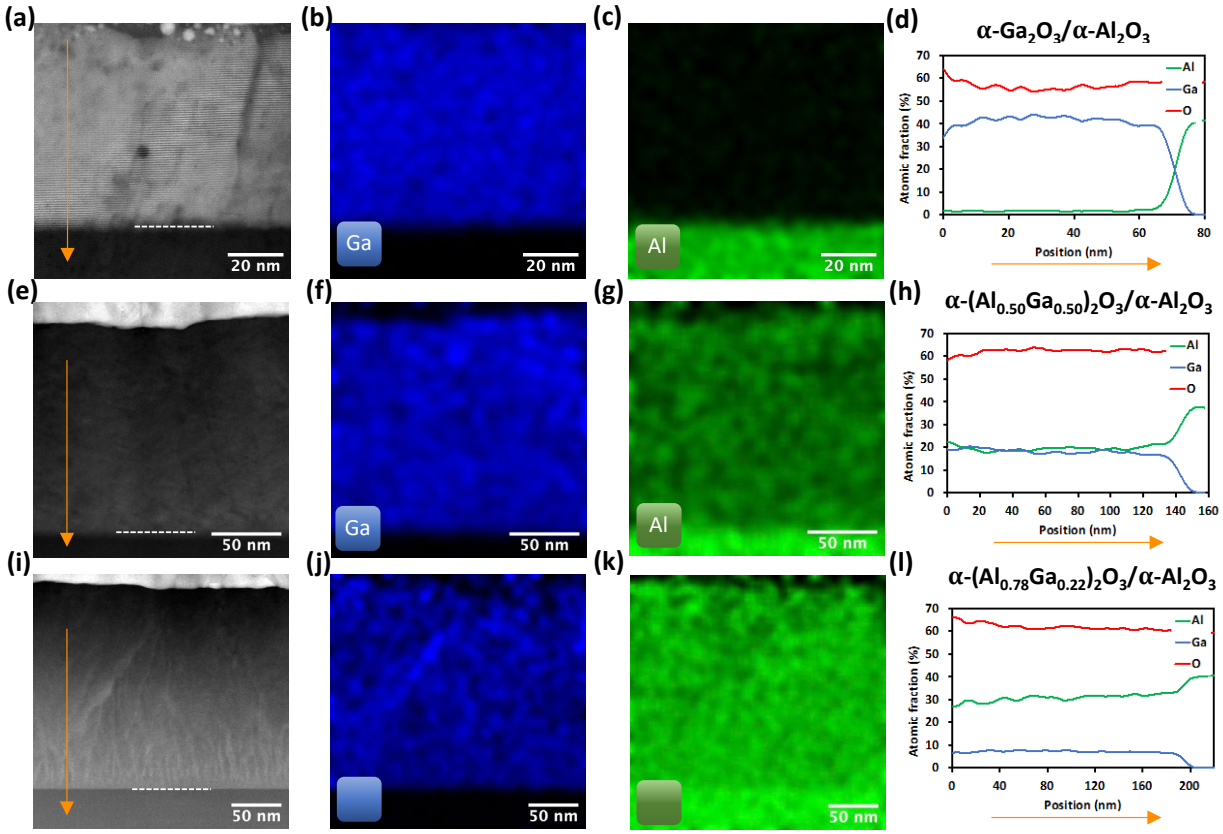

Figure 8. STEM-EDS mapping for (a-d) α-Ga_2O_3 and α-$(Al_xGa_{1-x})_2O_3$ films with (e-h) 50% and (i-l) 78% Al compositions. (a) HAADF images for (a) α-Ga_2O_3 and α-$(Al_xGa_{1-x})_2O_3$ films with (e) 50% and (i) 78% Al compositions with their corresponding (b, f, j) Ga and (c, g, k) Al EDS maps and (d, h, l) atomic fraction elemental profile as indicated by the orange arrows in (a, e, i).

Figure 9

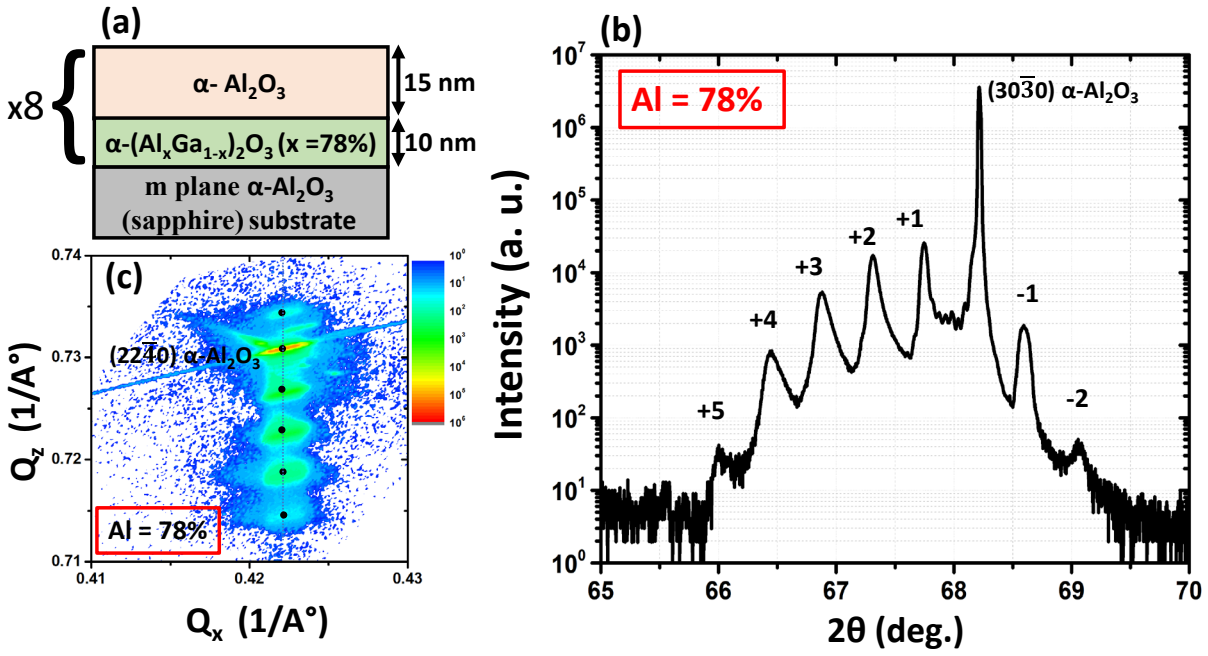

Figure 9. (a) Schematic of 8 period α-$(Al_xGa_{1-x})_2O_3$/α-Al_2O_3 superlattice structure grown with 78% Al composition in α-$(Al_xGa_{1-x})_2O_3$ layers; (b) XRD ω-2θ scan spectrum of the (30$\bar{3}$0) reflection; and (c) x-ray asymmetrical reciprocal space mapping (RSMs) around (22$\bar{4}$0) reflection of the SL structure with 78% Al composition.

Figure 10

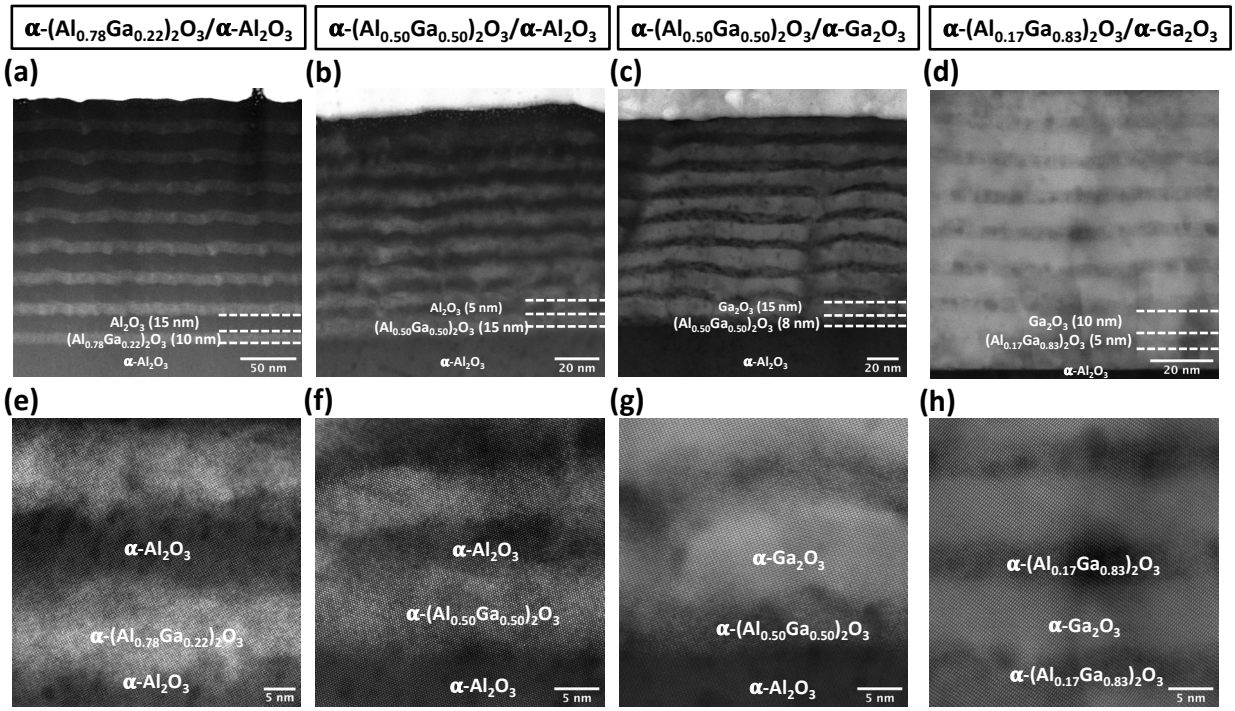

Figure 10. Atomic resolution cross-sectional HAADF-STEM images of 8 period α-$(Al_xGa_{1-x})_2O_3$/α-Al_2O_3 superlattice structures grown with (a, e) 78% and (b, f) 50% Al compositions. In addition, 8 period α-$(Al_xGa_{1-x})_2O_3$/α-Ga_2O_3 SL structures with (c, g) 50% and (d, h) 17% Al compositions are also shown with (a,b,c,d) 50 nm and (e,f,g,h) 2 nm scale. Corresponding layer thicknesses are included for different structures. The white dashed lines represent the substrate-epilayer interfaces. The HAADF-STEM images of α-$(Al_xGa_{1-x})_2O_3$/α-Al_2O_3 superlattice structures with 78% and 50% Al compositions were taken from $<24\bar{6}1>$ and <0001> zone axes, respectively. And both α-$(Al_xGa_{1-x})_2O_3$/α-Ga_2O_3 SL structures with 50% and 17% Al compositions were viewed along $<12\bar{3}\bar{1}>$ zone axes.

Figure 11

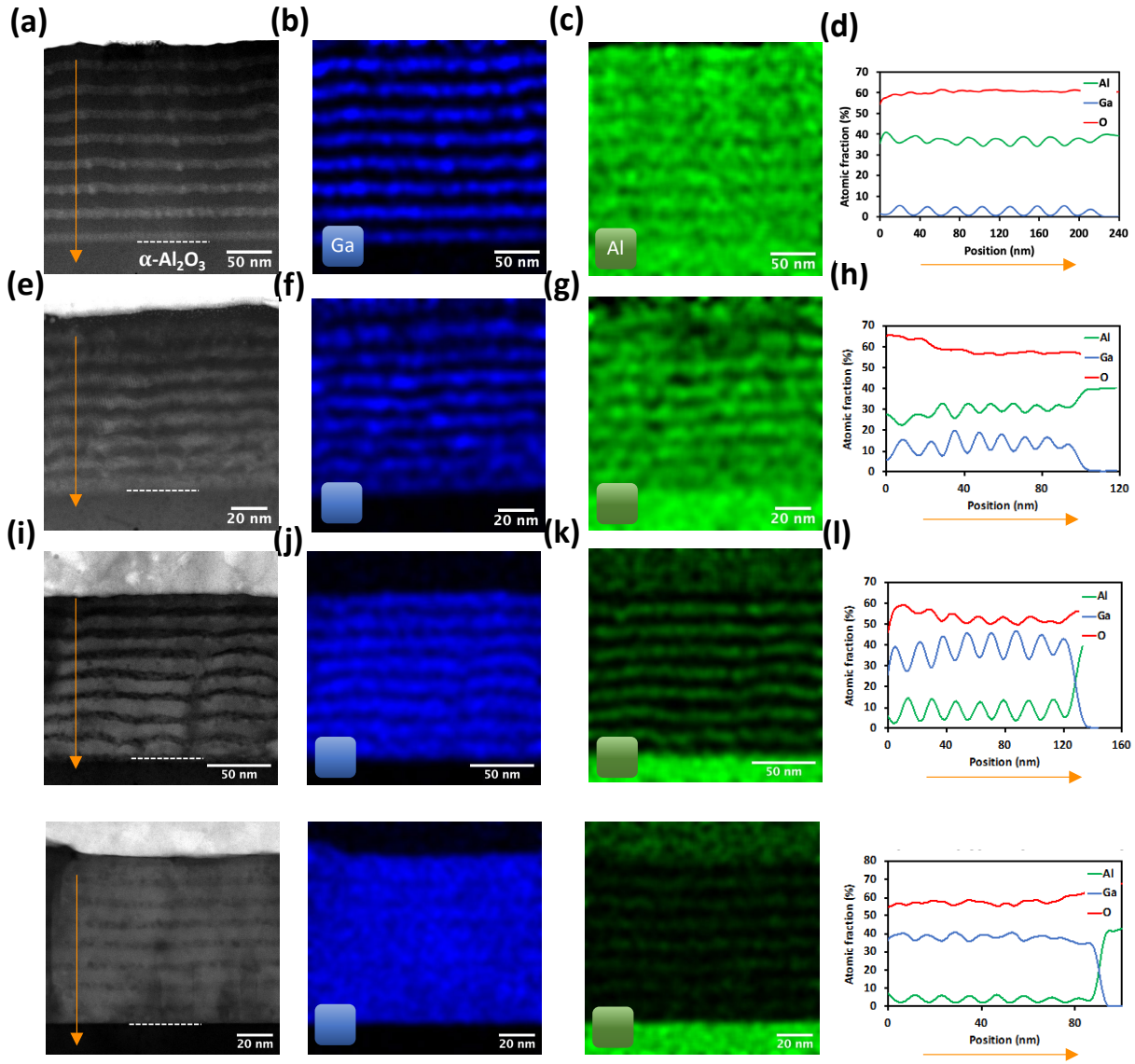

Figure 11. STEM-EDS mapping for α-$(Al_xGa_{1-x})_2O_3$/α-Al_2O_3 superlattice structures grown with (a-d) 78% and (e-h) 50% Al compositions and α-$(Al_xGa_{1-x})_2O_3$/α-Ga_2O_3 SL structures with (i-l) 50% and (m-p) 17% Al compositions. (a,e,i,m) HAADF images with their corresponding (b, f, j,n) Ga and (c, g, k,o) Al EDS maps and (d, h, l, p) atomic fraction elemental profile as indicated by the orange arrows in (a, e, i, m).

Figure 12

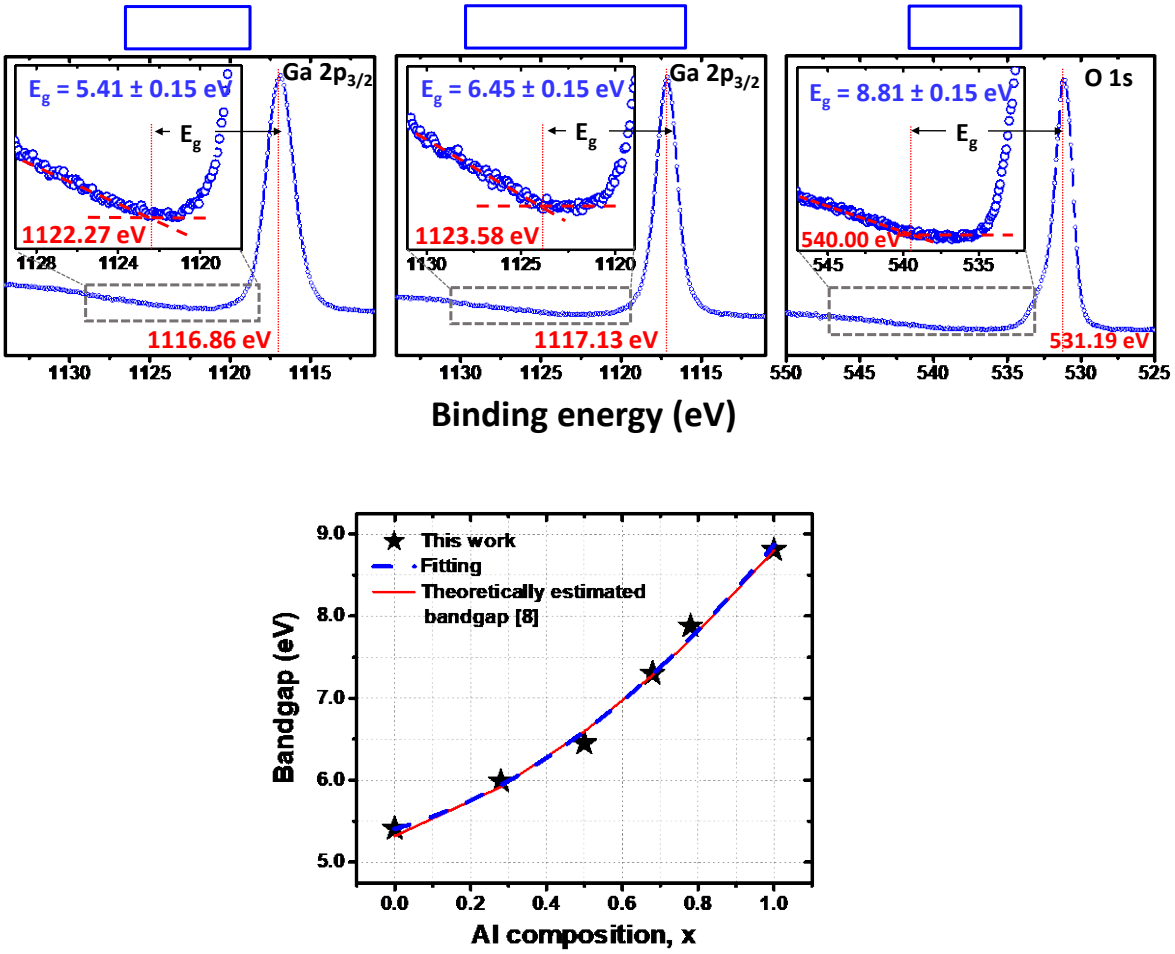

Figure 12. The bandgap energies of (a) α-Ga_2O_3, (b) α-$(Al_xGa_{1-x})_2O_3$ films with 50% Al composition and (c) α-Al_2O_3 films determined by calculating the energy difference between Ga $2p_{3/2}$ or O 1s core level peak and the onset of energy loss spectrum. The inset figures represent the zoomed view of the background region of the Ga $2p_{3/2}$ and O 1s core levels. (d) The bandgap energies of α-$(Al_xGa_{1-x})_2O_3$ films as a function of Al compositions, showing a good agreement with the theoretically predicted bandgap values.

Figure 13

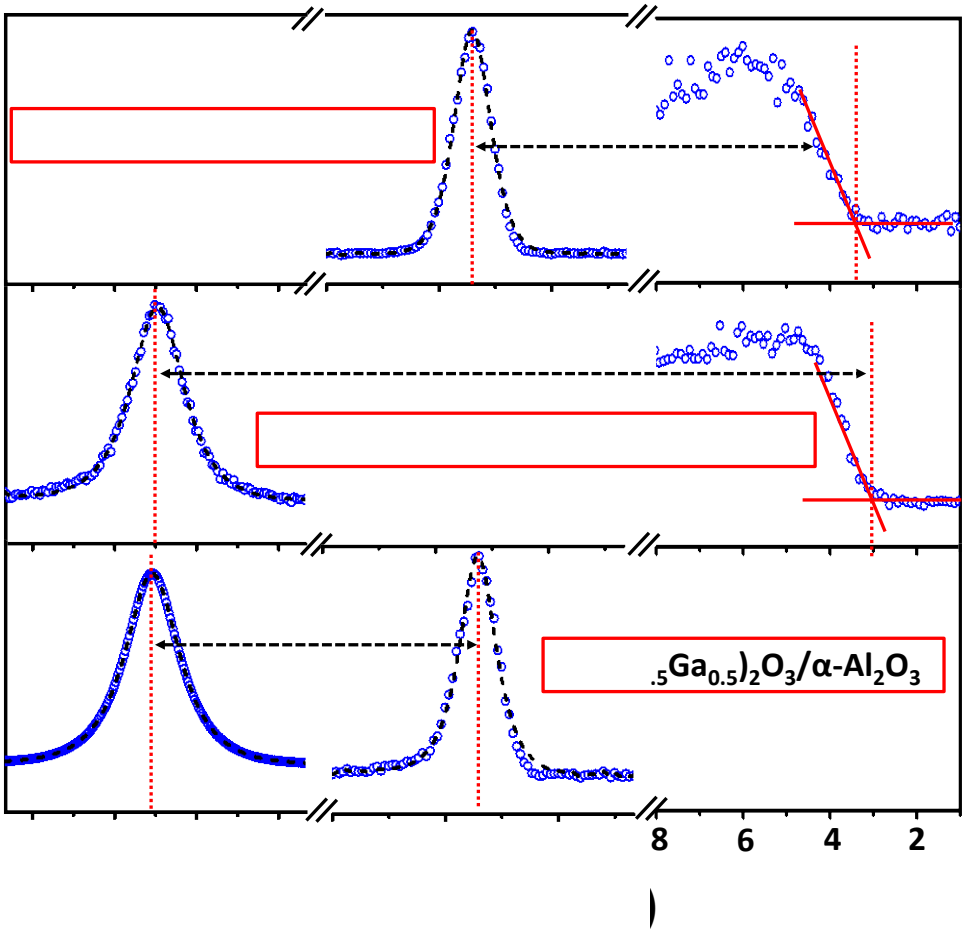

Figure 13. Al 2p and Ga 3s core-levels and valence band (VB) spectra from 50 nm thick (a) α-Al_2O_3 film (b) α-$(Al_xGa_{1-x})_2O_3$ film and (c) α-$(Al_xGa_{1-x})_2O_3$/α-Al_2O_3 interface with x = 0.50. Data are shown as blue open circles and the fitted curves are represented as black dashed lines for Ga 3s and Al 2p core-levels. Red solid straight lines represent the linear fitting of VB spectra of α-Al_2O_3 and α-$(Al_xGa_{1-x})_2O_3$ films.

Figure 14

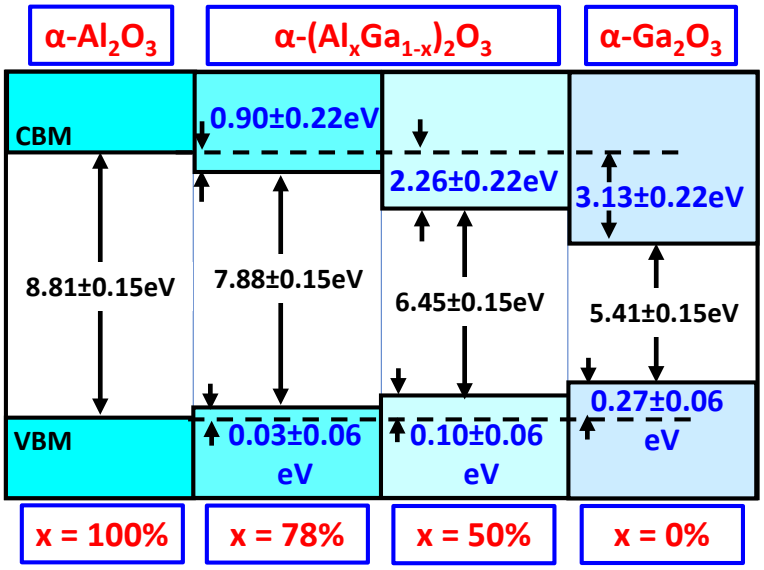

Figure 14. Summary of the valance and conduction band offsets at α-Al_2O_3/α-$(Al_xGa_{1-x})_2O_3$ interfaces with Al composition of 78%, 50% and 0%, The corresponding bandgap energies of α-$(Al_xGa_{1-x})_2O_3$ films for different Al compositions are also included.

Supplementary material

Metalorganic Chemical Vapor Deposition of α-Ga_2O_3 and α-$(Al_xGa_{1-x})_2O_3$ thin films on m-plane sapphire substrates

A F M Anhar Uddin Bhuiyan[1,a)], Zixuan Feng[1], Hsien-Lien Huang[2], Lingyu Meng[1], Jinwoo Hwang[2], and Hongping Zhao[1,2,b)]

[1]*Department of Electrical and Computer Engineering, The Ohio State University, Columbus, OH 43210, USA*

[2]*Department of Materials Science and Engineering, The Ohio State University, Columbus, OH 43210, USA*

[a)]Email: bhuiyan.13@osu.edu [b)]Corresponding author Email: zhao.2592@osu.edu

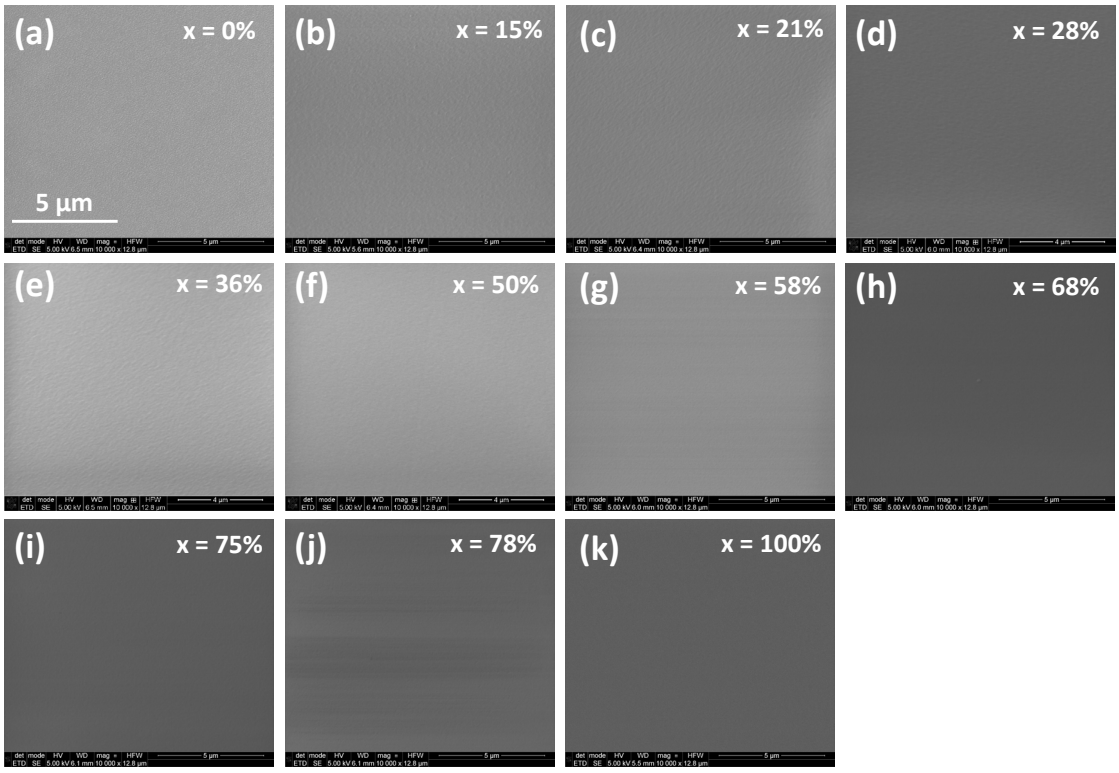

Figure S1 Surface view FESEM images of α-$(Al_xGa_{1-x})_2O_3$ films with different Al compositions.

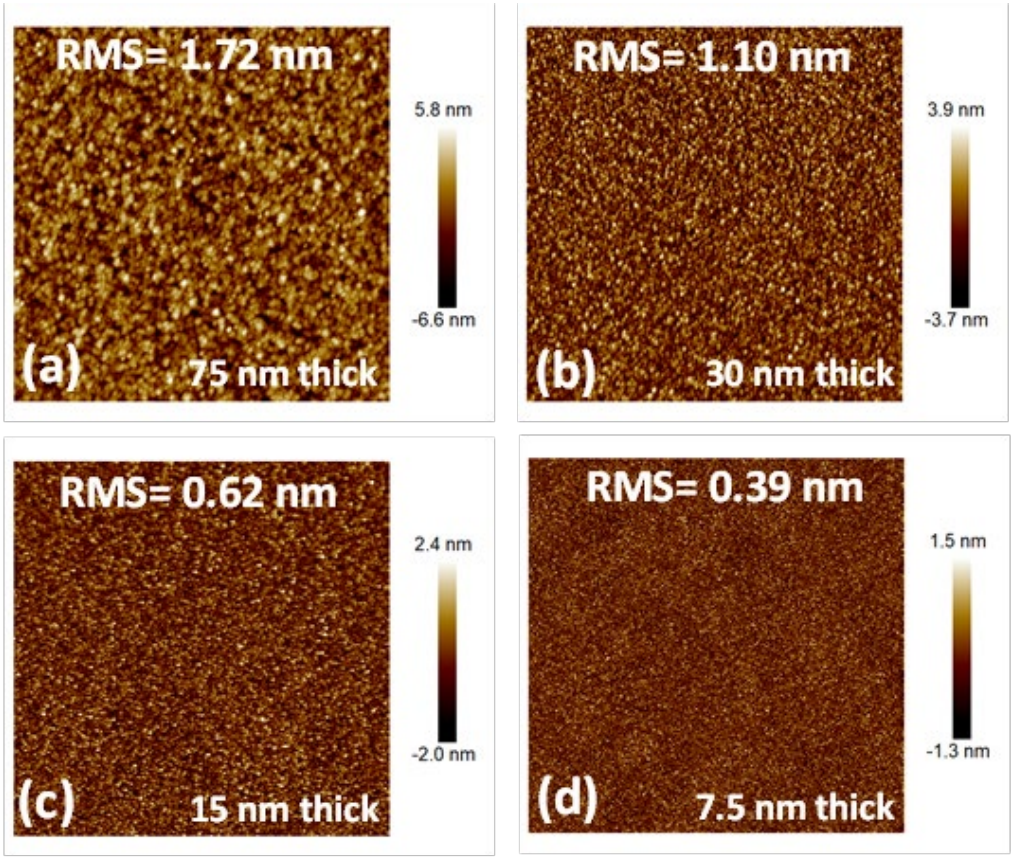

Figure S2 Surface AFM images of α-$(Al_{0.50}Ga_{0.50})_2O_3$ films grown with (a) 75 nm, (b) 30 nm, (c) 15 nm, and (d) 7.5 nm thicknesses.

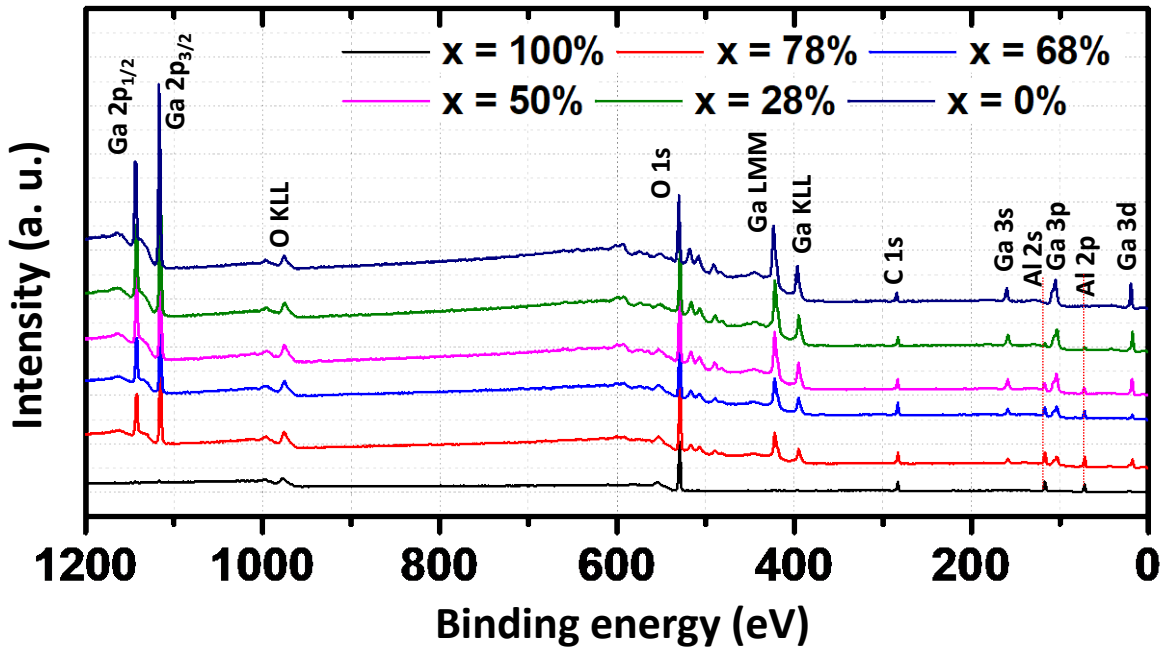

Figure S3. Survey spectra of α-$(Al_xGa_{1-x})_2O_3$ films with Al compositions of x = 0%, 28%, 50%, 68%, 78% and 100%.

Table S1

Summary of the calculated Al contents for α-$(Al_xGa_{1-x})_2O_3$ samples grown with different [TMAl]/[TMAl+TEGa] molar flow rate ratios (Table 1) by using the area of Ga 3s, Al 2s and Al 2p core levels with their respective sensitivity factors ($S_{Ga\ 3s}$ = 1.13, $S_{Al\ 2s}$ = 0.753, $S_{Al\ 2p}$ = 0.5371).

The Al compositions in the α-$(Al_xGa_{1-x})_2O_3$ samples were determined by comparing the areas for the Ga 3s with the Al 2s and Al 2p core level spectra by using below formula:

$$Al\ composition\ (\%) = 100\ X\ \frac{\frac{Area_{Al\ 2s}}{RSF_{Al\ 2s}}}{\frac{Area_{Ga\ 3s}}{RSF_{Ga\ 3s}} + \frac{Area_{Al\ 2s}}{RSF_{Al\ 2s}}}$$

Sample No.	[TMAl]/[TMAl+TEGa] (%)	$\frac{Area_{Ga\ 3s}}{RSF_{Ga\ 3s}}$	$\frac{Area_{Al\ 2s}}{RSF_{Al\ 2s}}$	$\frac{Area_{Al\ 2p}}{RSF_{Al\ 2p}}$	Al content (%) (By using Ga 3s and Al 2s core levels)	Al content (%) (By using Ga 3s and Al 2p core levels)	Al content (%) (XRD)
4	7.27	7739.2	3168.5	3300.9	29.05%	29.90%	28%
6	18.08	6740.1	6547.7	6861.3	49.28%	50.45%	50%
8	35.00	4299.0	7906.6	7792.8	64.78%	64.45%	68%
10	49.24	3568.7	10535.6	10353.8	74.70%	74.37%	78%

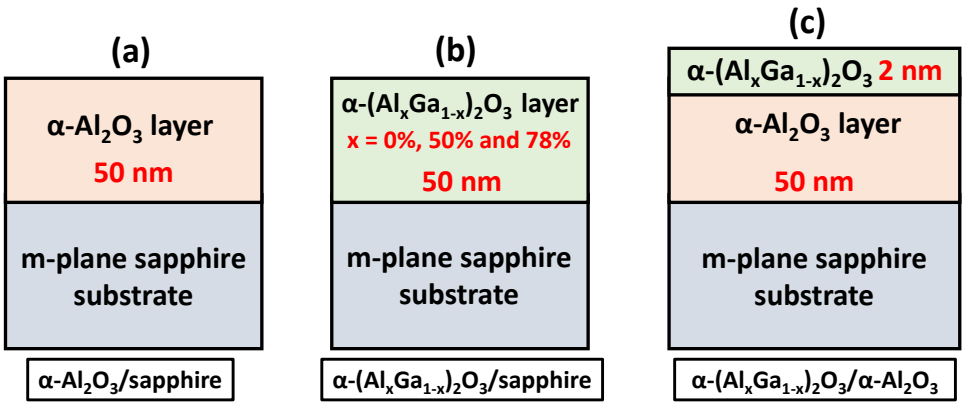

Figure S4 Schematic of (a) 50 nm thick α-Al_2O_3, (b) α-$(Al_xGa_{1-x})_2O_3$ films grown on m-plane sapphire substrate, and (c) 2 nm thick α-$(Al_xGa_{1-x})_2O_3$ films grown on top of 50 nm thick α-Al_2O_3 layer on m-plane sapphire substrate. The Al compositions in α-$(Al_xGa_{1-x})_2O_3$ films are tuned as 0%, 50% and 78%.